LUND UNIVERSITY

Master of Science Thesis

Optimisation of window settings for quantitative ^{111}In imaging – a comparison of measurements to Monte Carlo

Maria Holstensson

Supervisors: Cecilia Hindorf, PhD,
Prof. Michael Ljungberg and Glenn Flux, PhD.

This work has been performed at
Joint Department of Physics
The Royal Marsden NHS Foundation Trust
Sutton, UK

Medical Radiation Physics
Clinical Sciences, Lund
Lund University, 2006

Abstract

Quantification in Nuclear Medicine Imaging is highly desirable for a number of reasons. In Targeted Radionuclide Therapy for example, accurate estimation of the absorbed dose delivered to the patient depends upon accurately quantified images. In Tracer Kinetic Studies quantification is also required in order to obtain accurate biodistribution data. One of the major problems connected with Nuclear Medicine Imaging is scattered radiation. Photons emitted within the patient can be scattered by the patients themselves or by the collimator of the imaging system. This results in loss of energy and spatial information leading to degradation in image quality.

A widely used method for scatter correction is subtraction of images formed using energy windows in the region of the photopeaks. In this thesis a number of different energy window settings for the isotope ^{111}In are investigated using both phantom experiments and Monte Carlo simulations with the code SIMIND. Parameters used for comparison of the different window settings include; spatial resolution, sensitivity, image contrast, activity quantification and spill out. Also, the fraction of scattered photons in the detected spectra is investigated for the Monte Carlo modelled data and compared to the calculated experimental *Scatter to Total Ratios* for the various window settings.

For each of the scatter correction techniques experimental and Monte Carlo calculated results are tabulated and compared. The scatter correction techniques are then intercompared. Finally recommendations are made as to which is the best performing technique.

Summary for the general public in Swedish

Hitta den bästa kamerainställningen genom att både avbilda och modellera verkligheten

I Nukleärmedicin utnyttjas radioaktiva isotoper i både diagnostik och behandling för att kunna ta reda på var i kroppen ett visst läkemedel har tagit vägen. Det görs genom att man knyter isotopen till läkemedlet och detekterar strålningen som denna sänder ut när den sönderfaller i kroppen med en så kallad *scintillationskamera*. Denna teknik används ofta för läkemedel som söker sig till tumörer, just för att man vill veta var tumörerna finns i kroppen. Ofta knyts också en andra isotop till läkemedlet som utsänder en annan slags strålning i syfte att förgöra tumören. Under en sådan behandling är det oerhört viktigt att tillräckligt mycket strålning når tumörerna så att de verkligen utplånas, men det är samtidigt lika viktigt att inget annat livsnödvändigt friskt organ i kroppen skadas av strålningen så att det upphör att fungera. Det är här scintillationskameran kommer till användning: genom att ta bilder av patienten som får behandlingen kan man beräkna hur mycket av läkemedlet som har tagits upp på olika ställen i kroppen.

Det finns dock problem förknippade med denna typ av bildtagning. Strålningen som sänds ut från olika ställen i kroppen kan både absorberas och spridas i kroppen. Den absorberade strålningen når aldrig kameran och detekteras således inte. Den spridda strålningen kan detekteras, men ger falsk information i kameran om sitt ursprung. För att få *kvantitativt riktiga* bilder måste dessa effekter korrigeras för. Vid bildtagning med en scintillationskamera sätts ett så kallat energifönster över den energi som strålningen har, kallat huvudfönstret. I detta huvudfönster kommer alltid en viss mängd spridd strålning att hamna. Därför används ofta så kallade spridningsfönster vid sidan av huvudfönstret för att uppskatta mängden spridd strålning i bilden.

Syftet med detta arbete var att hitta de bästa fönstersättningarna vid bildtagning av isotopen 111-indium för en scintillationskamera på *The Royal Marsden Hospital* i London. För detta gjordes både experimentella mätningar med kameran och simuleringar av kameran med ett Monte Carlo-baserat program vid namn SIMIND. Monte Carlo-simuleringar används för fenomen som varierar slumpmässigt, vilket sönderfallet av isotoperna i kroppen gör. Fördelen med dessa simuleringar är bland annat att de kan tala om vilka händelser i bilden som kommer från spridd strålning vilket man inte kan mäta. I denna studie jämfördes tio olika fönstersättningar med avseende på flera olika parametrar som är viktiga vid kvantitativ bildtagning.

Table of contents

1. Introduction

In Nuclear Medicine radioisotopes are used in the diagnosis and treatment of cancer. For diagnosis and staging, tracer amounts of radiopharmaceuticals are injected and the biodistribution is studied [1]. In *Targeted Radionuclide Therapy* (TRT), very large amounts of activity are administered with the aim of either a palliative or curative treatment. In all these applications, accurate determination of the spatial distribution as a function of time and accurate absolute quantification of the radiopharmaceutical uptake are highly desirable. In TRT accurate knowledge of the activity distribution is essential for dosimetry in order to assess dose-response-relationships. At the same time as complete remission of the diseased tissue is desirable, radiotoxicity of other organs and tissues at risk must be avoided [2, 3]. Individual planning of each patient's TRT is needed since the biokinetics of the radiopharmaceutical differ from patient to patient.

Nuclear Medicine imaging produces representations of activity distributions within the body by detecting the photons emitted due to decay of the tracer [4]. In scintillation camera imaging the quality of the images, and therefore the accuracy of the quantification, is limited by several factors. Firstly, there are the performance limitations of the camera such as the spatial resolution and energy resolution. The spatial resolution refers to the ability of the camera to provide sharpness or detail to the image and comprises of intrinsic and extrinsic components. Intrinsically, the spatial resolution is limited due to statistical variations in the distribution of light photons in the detection process The extrinsic spatial resolution is limited by the collimator, which is used to define the direction of the detected photons. Energy resolution refers to the camera's ability to resolve fine detail in the incident energy of the photons and is limited by random statistical variations in the events leading to the formation of an output signal [5, 6]. A good energy resolution improves the spatial resolution since it helps in discriminating scattered photons.

Secondly, the images are degraded by attenuation and scatter of the photons emitted in the patient. The desirable photons in scintillation camera imaging are the ones that escape the patient with no change of energy or direction, so called primary photons. An attenuated photon never reaches the detector as it is absorbed within the body of the patient or in the collimator. A scattered photon is a photon that has interacted with the matter in the patient's body or in the collimator and hence been deflected from its initial path and lost energy. The limited energy resolution of scintillation detectors is not sufficient to discriminate all scattered photons from unscattered ones. As a result, scattered photons are often included in the image and cause a blurring effect [4].

The image degrading factors mentioned above depend on the energy of the photons emitted. Therefore the energy window setting used when imaging patients is crucial for the image quality. Since scattered photons will be detected in the main window (the energy window around the photopeak) used to create the image, the settings of additional energy windows for accurate scatter estimation is also essential. Subtraction of the estimated scatter contribution from the measured projections is a widely used scatter correction method [7].

The aim of this study was to evaluate different window settings and correction methods for ^{111}In imaging on a Philips FORTE scintillation camera preparatory to an upcoming tracer kinetic study. In this study an ^{111}In labelled monoclonal antibody will be used to predict the in vivo behaviour of the high-energy pure β^- particle emitting isotope ^{90}Y, also labelled to a monoclonal antibody. Since ^{90}Y is not suitable for quantitative imaging ^{111}In is commonly used as a surrogate in tracer kinetic studies. It is known that differences exist in the biodistribution of a tracer when different radionuclides are labelled to it. However, several studies have shown that ^{111}In and ^{90}Y have almost identical biodistribution patterns when labelled to the same antibody [8, 16, 17, 18].

The approach for evaluation of different window settings was a combination of physical phantom experiments and Monte Carlo simulations. By the use of Monte Carlo simulations effects of parameters that cannot be measured experimentally, such as the fraction of photons that are scattered in a phantom and their contribution to the image, were studied [4]. In the simulations, effects in the phantom, such as photon attenuation and scatter, could be 'turned off' which means that ideal images that include camera-specific parameters were created and used as reference images. By comparing the scatter- and attenuation-compensated images with this ideal image the accuracy of correction methods was investigated.

2. Materials and methods

In this section the acquisition, processing and evaluation of experimental and simulation data is described. In both experiments and simulations, images with different window settings and corresponding scatter corrections were obtained. The images were evaluated and compared to each other on the basis of a number of parameters.

2.1 Choice of window settings

The Philips FORTE scintillation camera, on which the energy windows were to be evaluated, has two detector heads and a maximum of three energy windows to be used during a study.

^{111}In is an artificial radioactive isotope of indium with a half-life of 2.80 days. It decays exclusively by electron capture, emitting primarily two gamma rays with the energies 171 keV and 245 keV [9]. Due to downscatter from the 245 keV photons, there is more scatter in a window centred over the 171 keV photopeak than in a window centred at 245 keV. There is no scatter at energies beyond the 245 keV photopeak.

From a qualitative imaging point of view it would be preferable to use an energy window centred over the 245 keV photopeak with two adjacent 'scatter windows' for *Triple Energy Window* (TEW) scatter correction (see description in section 2.3.1.1), seeing that it is the 'cleanest' of the two, and seeing that the energy resolution gets better and the attenuation less significant for higher energies. On the other hand, higher energies imply less probability for detection in the scintillation crystal and more septal penetration (photons passing through the collimator septa). Using only one photopeak also implies a poorer absolute signal level (cps/MBq) compared to using both photopeaks. A high absolute signal level is desirable in order to lower the signal to noise ratio (SNR) and/or the acquisition time.

Owing to the fact that there is a maximum of three energy windows during a study, it is not possible to simultaneously use both photopeaks with TEW scatter correction. Instead, if both photo peaks are to be included in the image, the scatter needs to be estimated from *One Scatter Window* (OSW).

In this study ten different combinations of window settings for ^{111}In imaging were evaluated, using the photopeaks both one by one and altogether. Window settings with both TEW and OSW scatter corrections were used, as well as window settings with *No Scatter Correction* (NSC). In Table 1 below these window settings are shown and described. The spectrum is taken from a homogenous water filled phantom with an ^{111}In source in the centre. In the

spectrum, the solid blue lines indicate the main energy windows; the pink dotted lines indicate the scatter windows and the yellow area illustrates the counts deleted after scatter correction.

Table 1. An overview of the window settings evaluated in this study. The solid blue lines indicate the main energy windows; the pink dotted lines indicate the scatter windows and the yellow area illustrates the counts deleted after scatter correction.

NSC_171	**TEW_171**
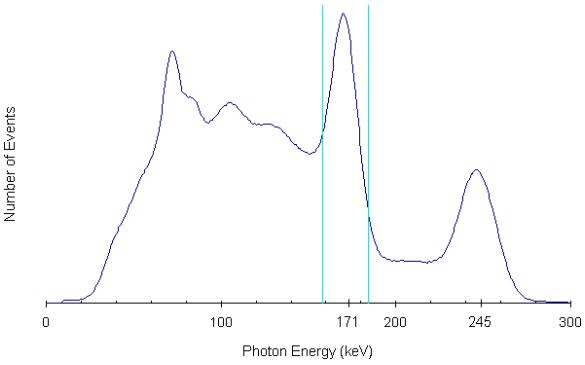	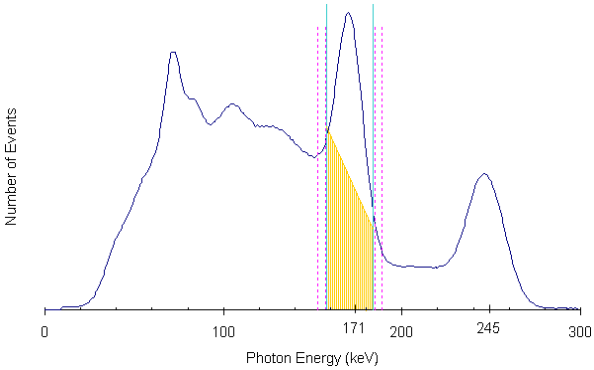
Window setting *NSC_171*: A 15 % energy window over The 171 keV photopeak with No Scatter Correction (NSC).	Window setting *TEW_171*: A 15 % energy window over the 171 keV photopeak together with two adjacent 2 % scatter windows for TEW scatter correction.
NSC_245	**TEW_245**
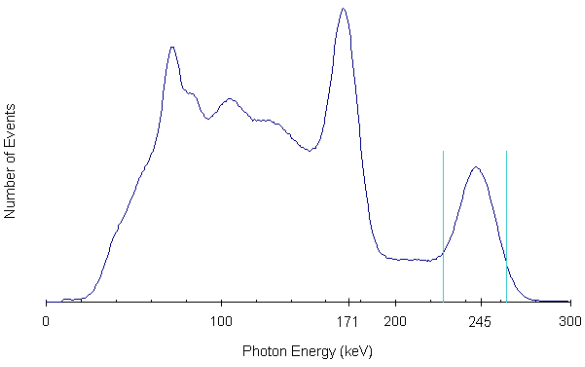	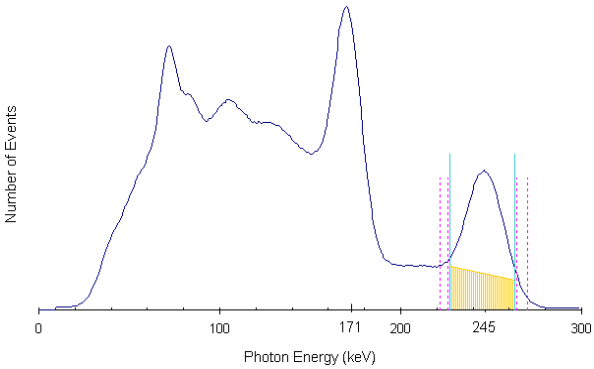
Window setting *NSC_245*: A 15 % energy window over The 245 keV photopeak without scatter correction.	Window setting *TEW_245*: A 15 % energy window over the 245 keV photopeak together with two adjacent 2 % scatter windows for TEW scatter correction.

NSC_171_245

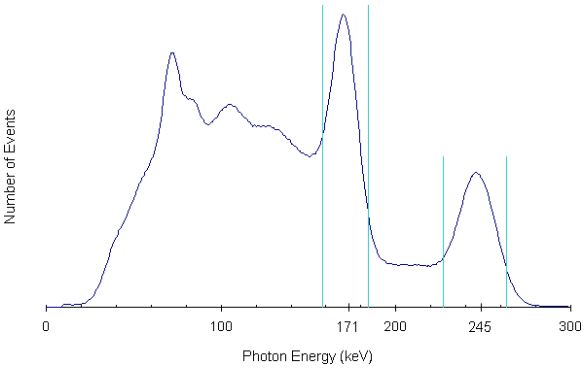

Window setting *NSC_171_245*: A 15 % energy window over the 171 keV photopeak together with a 15 % energy window over the 245 keV photopeak without scatter correction.

OSW_A_171_245

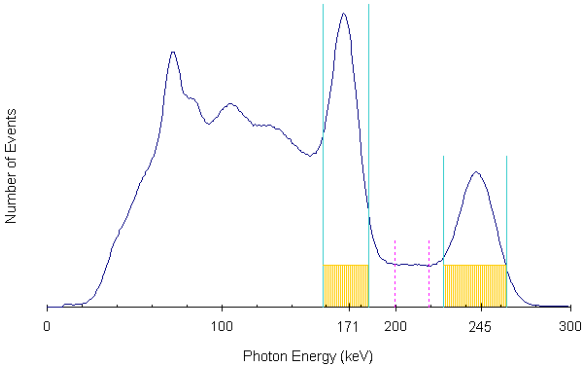

Window setting *OSW_A_171_245*: A 15 % energy window over the 171 keV photopeak together with a 15 % energy window over the 245 keV photopeak and a 10 % scatter window centred at 209 keV. The scatter in both main windows is assumed to be the same as in the scatter window. OSW stands for *One Scatter Window*.

OSW_B_171_245

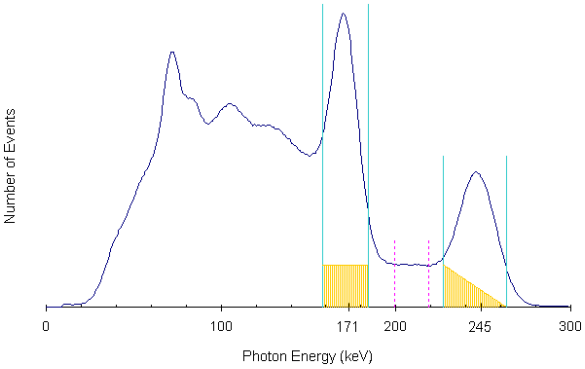

Window setting *OSW_B_171_245*: A 15 % energy window over the 171 keV photopeak together with a 15 % energy window over the 245 keV photopeak and a 10 % scatter window centred at 209 keV. The scatter in the 171 keV window is assumed to be the same as in the scatter window. A TEW scatter correction is applied to the 245 keV window after the assumption that there is no scatter to the right of it.

OSW_EXT_171_245

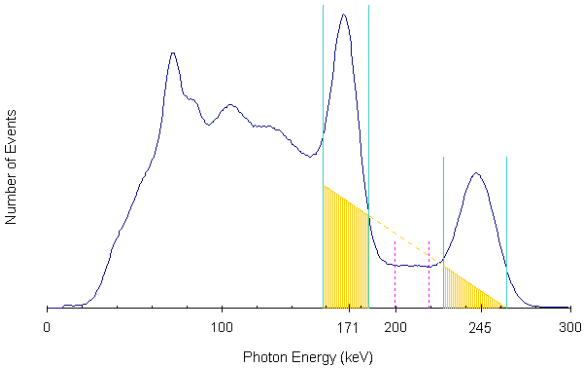

Window setting *OSW_EXT_171_245*: A 15 % energy window over the 171 keV photopeak together with a 15 % energy window over the 245 keV photopeak and a 10 % scatter window centred at 209 keV. A TEW scatter correction is applied to the 245 keV window after the assumption that there is no scatter to the right of it. The function is extrapolated to the 171 keV window for scatter correction. EXT stands for *Extrapolated*.

NSC_211

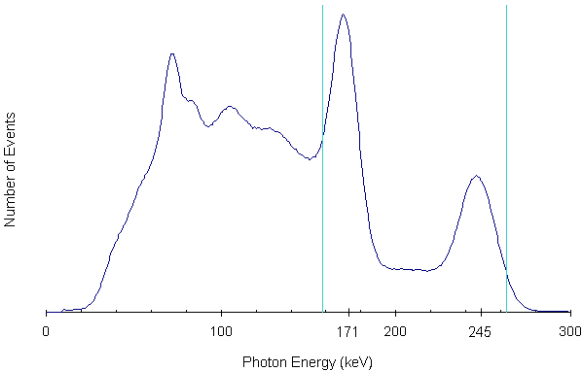

Window setting *NSC_211*: A 50 % energy window centred at 211 keV without scatter correction.

TEW_211

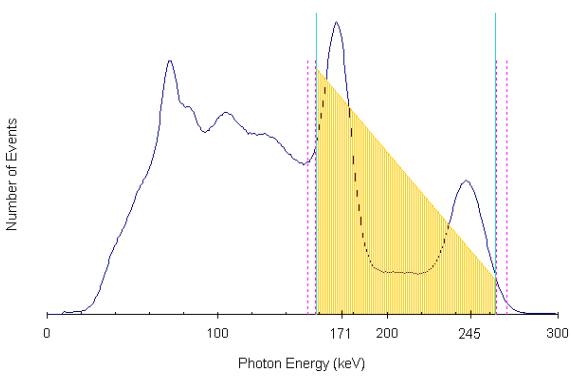

Window setting *TEW_211*: A 50 % energy window centred at 211 keV together with two adjacent 2 % scatter windows for TEW scatter correction.

2.2 List mode acquisitions

All experimental acquisitions were carried out on the Philips FORTE camera in *list mode*. In list mode acquisition, the incoming X- and Y-position coordinates of each event within the camera are stored in a list, instead of being immediately formed into an image matrix. Periodic timing marks at millisecond intervals are also included in the list. After acquisition the list mode data can be processed and reformatted into conventional images with specific number of counts, window settings and matrix sizes. The advantage of list-mode acquisition is that it allows greater flexibility for data analysis, which was desirable in this study [6, 10]. List mode acquisition also makes it possible to create spectrum files. This was done in order to be able to compare spectra from the experiments and simulations.

2.2.1 List mode data processing

The list mode data was processed using *The Royal Marsden Dosimetry Package* (RMDP). The data from detector head one and two were processed separately. First an energy calibration was made using the 171 keV photopeak. Subsequently the number of events to process, matrix size, window centres and widths were specified. The window centres and widths for the images created are specified in Table 2.

Table 2. The window settings for the images created from the list mode data using RMDP.

Window centre (keV)	Window width (%)	Window width (keV)
155	2	5
171	15	27
187	2	5
209	10	21
224	2	5
211	50	107
245	15	37
267	2	7
171+245 [1]	15	27+37

[1] Both photopeaks were fused in to one image.

2.3 Image processing

The images created by simulation and by RMDP from the list mode data, as described in section 2.4 and 2.2.1 respectively, were read into IDL (*Interactive Data Language*, Research Systems, Inc. USA) for processing. The images originating from detector head two were reversed in order to turn them the same way around as the images originating from detector head one. An IDL routine was written to perform the scatter and attenuation corrections described below. The program can be found in Appendix 1.

2.3.1 Scatter correction

2.3.1.1 Triple Energy Window

In a typical TEW scatter correction the number of scattered photons in the photopeak window is determined by calculating the area of the trapezoid underneath the line joining the two adjacent scatter windows in the spectrum [11]. However, in this study a modification of the customary TEW scatter correction was used, in which the fact that the fraction of primary photons in the upper scatter window is higher than in the lower one is taken into consideration. In this modified version the scatter images were weighted with respect to the total number of counts they contained before calculating the area of the trapezoid. For the window settings *TEW_171*, *TEW_245* and *TEW_211* this modified TEW scatter correction was applied. Firstly the fractions that the low and the high scatter window possessed, f_{low} and f_{high} respectively, were calculated as

$$f_{low} = \frac{C_{low}/w_{low}}{(C_{low}/w_{low}) + (C_{high}/w_{high})}$$ Equation 2-1

$$f_{high} = 1 - f_{low}$$ Equation 2-2

where C_{low} and C_{high} are the total number of counts in the low and high energy scatter windows respectively, and w_{low} and w_{high} are the widths (in keV) of the low and high energy scatter windows respectively. The TEW scatter corrected image, IMA_{main}^{TEW}, was then created as

$$IMA_{main}^{TEW} = IMA_{main} - \left(\left(IMA_{low} \cdot f_{low} \cdot \frac{w_{main}}{w_{low}} \right) + \left(IMA_{high} \cdot f_{high} \cdot \frac{w_{main}}{w_{high}} \right) \right)$$ Equation 2-3

where IMA_{main} is the photopeak image, IMA_{low} and IMA_{high} are the low and high energy scatter images respectively and w_{main} is the width of the photopeak window (in keV).

2.3.1.2 One Scatter Window

For the window settings *OSW_A_171_245*, *OSW_B_171_245* and *OSW_EXT_171_245* the scatter in the 171 keV and 245 keV windows was estimated from one single scatter window in between the two photopeaks, centred at 209 keV. For these window settings the 171 and 245 keV images were scatter corrected separately before fusing the two into one image.

For window setting *OSW_A_171_245* the scatter in both main windows was assumed to be the same as in the scatter window. The scatter correction was made as

$$IMA_{171}^{OSW\_A} = IMA_{171,main} - \left(IMA_{209} \cdot \frac{w_{171,main}}{w_{209}} \right)$$ Equation 2-4

$$IMA_{245}^{OSW\_A} = IMA_{245,main} - \left(IMA_{209} \cdot \frac{w_{245,main}}{w_{209}} \right)$$ Equation 2-5

$$IMA_{171+245}^{OSW\_A} = IMA_{171}^{OSW\_A} + IMA_{245}^{OSW\_A}$$ Equation 2-6

where $IMA_{171,main}$ and $IMA_{245,main}$ are the uncorrected photopeak images, IMA_{209} is the scatter image, $w_{171,main}$ and $w_{245,main}$ are the widths (in keV) of the 171 and 245 keV photopeak windows respectively and w_{209} is the width (in keV) of the scatter window.

For window setting *OSW_B_171_245* the scatter correction applied to the 171 keV image was the same as in Equation 2-4. But for the 245 keV window the assumption is made that there is no scatter beyond the upper window boundary. Hence a 'triple energy window' scatter correction was applied to the 245 keV image:

$$IMA_{245}^{OSW\_B} = IMA_{245,main} - \left(IMA_{209} \cdot \frac{w_{245,main} / w_{209}}{2} \right) \qquad \text{Equation 2-7}$$

$$IMA_{171+245}^{OSW\_B} = IMA_{171}^{OSW\_A} + IMA_{245}^{OSW\_B} \qquad \text{Equation 2-8}$$

For window setting *OSW_EXT_171_245* the 'triple energy window' scatter correction described in Equation 2-7 was applied to the 245 keV photopeak and extrapolated back to the 171 keV window. If the number of scatter counts in energy channel 158 (the lower boundary of the 15 % energy window centred at 245 keV) is a, and 0 in energy channel 184 (the upper boundary of the 245 keV energy window) then interpolation gives that the number of scatter counts in channel 171 is $2.56 \cdot a$:

$$IMA_{171}^{OSW\_EXT} = IMA_{171,main} - \left(IMA_{209} \cdot \frac{w_{171,main}}{w_{209}} \cdot 2.56 \right) \qquad \text{Equation 2-9}$$

$$IMA_{171+245}^{OSW\_EXT} = IMA_{171}^{OSW\_INT} + IMA_{245}^{OSW\_B} \qquad \text{Equation 2-10}$$

After scatter correction all negative pixel values were set to zero.

2.3.2 Attenuation correction

Attenuation correction was done with the *Geometrical Mean* (GM) method, which requires opposing images either side of the volume of interest. Assuming narrow beam geometry, the count-rates in the anterior and posterior views, R_A and R_P respectively, are given by

$$R_A = R_0 \cdot e^{-\mu_A \cdot d} \qquad \text{Equation 2-11}$$

$$R_P = R_0 \cdot e^{-\mu_P \cdot (T-d)} \qquad \text{Equation 2-12}$$

where μ_A and μ_P are the linear attenuation coefficients for the anterior and posterior views respectively, d is the depth to the source from the anterior view, T is the thickness of the object that is being imaged and R_0 is the emitted count rate. A sketch with the parameters drawn in is shown in Figure 1.

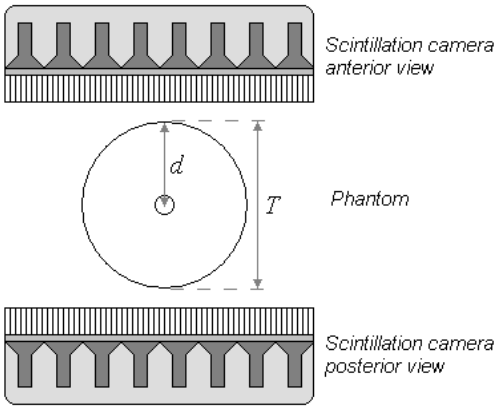

Figure 1. *The two detector heads of the gamma camera with a phantom in between. The thickness of the phantom is* T *and the depth to the source from the anterior view is* d.

When adding Equation 2-11 and 2-12 together and assuming a common linear attenuation coefficient for the two views, μ, the dependence of d disappears and the emitted count rate can be calculated as

$$R_0 = \frac{\sqrt{R_A \cdot R_P}}{e^{-\mu \cdot \frac{T}{2}}} \qquad \text{Equation 2-13}$$

Applying the GM attenuation correction on the images, 'count rate images' *GM_IMA* were created using the images from both detector heads:

$$GM\_IMA = \frac{\sqrt{IMA_{H1} \cdot IMA_{H2}} \Big/ t_{acq}}{e^{-\mu \cdot T/2}} \qquad \text{Equation 2-14}$$

where IMA_{H1} and IMA_{H2} are the images from detector head one and two respectively, t_{acq} is the acquisition time, μ is the linear attenuation coefficient and T is the thickness of the phantom. The linear attenuation coefficients used were 0.145 cm^{-1} (171 keV window), 0.135 cm^{-1} (211 keV and 171+245 keV windows) and 0.129 cm^{-1} (245 keV window).

A narrow bean attenuation correction can be applied if a proper scatter correction has been made [6]. The correction can also be applied in regions with non-homogeneous attenuation if information about the attenuation distribution can be obtained (for example from a transmission study or a X-ray CT). The NSC (*No Scatter Correction*) images have not been scatter corrected but are simply included for completeness as a comparison to the images that have been scatter corrected. Some of the phantoms used do have more complex source distributions and the narrow beam geometry attenuation correction will therefore not be exact. However, exactly the same attenuation correction is applied to both experimental and modelled data. Since the main interest is the direct comparison within and between these datasets, any approximation made in the attenuation correction will be identical in every case.

2.4 SIMIND simulations

In this study, the Monte Carlo simulation code SIMIND (*SIMulation of Imaging Nuclear Detectors*) was used to simulate projection data of the phantoms described in sections 2.5.1-2.5.4. The program has been developed by Professor Michael Ljungberg at the Department of Medical Radiation Physics, Lund University, Sweden. SIMIND describes clinical scintillation cameras and can easily be modified for almost any type of calculation or measurement encountered in SPECT (*Single Photon Emission Tomography*) and planar imaging [12]. The program is based on the use of uniformly distributed random numbers for modelling the processes of the different photon interactions. It simulates the passage of photons through a phantom and collimator towards the detector crystal and calculates the projections. As in reality, the detection of the photons is affected by attenuation, scatter, the collimator and characteristics of the scintillation crystal among other things. Septal penetration and

characteristic x-rays, emitted from photoelectric absorption in the collimator, can also be simulated if desired [13].

SIMIND consists of two main programs, named CHANGE and SIMIND. The modification of the camera and collimator parameters and geometry, that is to be simulated, is made in CHANGE. SIMIND then reads the input files created by CHANGE and performs the actual Monte Carlo simulation. The output results are saved in a set of external data files [13]. The advantage of this Monte Carlo simulation is that it calculates parameters that are not directly measurable in experimental measurements, such as the *Scatter to Total ratio* (S/T) which is the fraction of the detected photons that are scattered, owing to the fact that the program can tell whether a detected photon is primary or scattered.

The phantoms simulated (see Figure 2-4 and 6) are representations of the phantoms used in the experimental acquisitions. The phantoms were created in IDL and represented by two binary maps describing the density and source distribution respectively. These files were read in to CHANGE to be simulated.

The simulations were performed for the Philips FORTE gamma camera equipped with an ADAC MEGP (Medium Energy General Purpose) collimator. The specifications and performance parameters of the camera, shown in Table 3, are taken from the acceptance tests done when the camera was purchased in the year 2000. The SIMIND program was installed on a number of different computer platforms and the results were validated. The simulations were calculated with 1 million photons per projection. Owing to the fact that SIMIND uses several variance reduction techniques, such as forced interaction and detection (which is then compensated by a proper calculated photon history weight) 1 million simulated photons provide better statistics than an experiment with 1 million emitted photons.

Table 3. *The characteristics of the Philips FORTE gamma camera and the MEGP collimator used in SIMIND.*

Scintillation crystal		
Length	38.100	cm
Width	50.800	cm
Thickness	9.520	mm
Intrinsic spatial resolution at 140 keV CFOV FWHM	3.120	mm
Energy resolution at 140 keV	9.500	%
Matrix size	128×128(1)	pixels
Pixel size	0.467(1)	cm

Distance between centre of phantom and surface of collimator	12.000	cm
ADAC Forte MEGP collimator		
Type	Parallel-hole	
Shape	Hexagonal	
Hole diameter	2.950	mm
Septal thickness	1.143	mm
Hole length	4.800	cm

(1) Except for the system spatial resolution simulations where the matrix size was 256×256 pixels and the pixel size was 0.234 cm.

For the energy resolution and intrinsic spatial resolution reference points were given as FWHM at 140 keV. The performances were then modelled from an 'on-line' convolution of the imparted energy (E) from each photon history by an energy dependent Gaussian function varying with $1/\sqrt{E}$. The energies of the photons emitted from ^{111}In that were simulated and their probability of each emission (branching fraction) were taken from *ENSDF Decay Data in the MIRD Format* (http://www.nndc.bnl.gov/mird). The window settings for the simulated images were the same as those described in Table 2.

For all windows simulated 'total', 'primary' and 'air' images were created. The 'total' images consist of both primary and scattered photons just as in experimental images. The 'primary' images contain only the primary photons. By subtracting the 'primary' images from the 'total' images in IDL, 'scatter' images were obtained. For the 'air' image no interactions have occurred in the phantom. This 'air' image therefore represents the ideal image to achieve after scatter and attenuation correction has been applied to the 'total' image.

In order to see how well the structures in the phantom described in section 2.5.3 were resolved in the processed simulated images, profiles were drawn and compared to the profiles of the 'air' images.

In the simulations binary energy spectra files were created in which the primary and scattered photons are separated. Also values of the scatter to total ratios (S/T) were given. These S/T values, which are assumed to be true, were compared to the calculated S/T values for the different scatter corrections applied. The calculated S/T values were obtained by dividing the number of photons deleted with the scatter correction, by the total number of photons in the images before scatter correction. The spectra from experimental acquisitions and simulations were compared visually.

2.5 Experimental acquisitions and image evaluation

In the sections below the phantoms, experimental acquisitions and the evaluation of the experimental and simulated images are described.

2.5.1 System planar sensitivity

The system planar sensitivity, S_{system}, (henceforth simply referred to as sensitivity) is the ratio of counts per unit time detected in one acquisition plane to the activity of a specific planar source placed parallel to that plane [14]. As the planar sensitivity depends on the window width and gamma energy among other things a specific value was needed for each window setting in order to be able to quantify the activity in the images.

Figure 2 shows the square phantom that was used for these measurements and simulations. The outside measurements of the phantom, made of Perspex, are 11.0×11.0×1.0 cm^3 and the inside measurements are 10.0×10.0×0.5 cm^3.

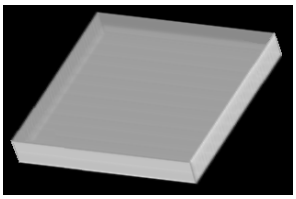

Figure 2 a. *The square phantom used for the system planar sensitivity measurement.*

b. *A transverse plane/sagittal plane of the square phantom.*

c. *A coronal plane of the square phantom.*

The phantom was uniformly filled with an activity of 10 MBq ^{111}In chloride and placed at the centre of the field of view at the distance 10 cm from the face of the collimator. 5 million counts for the whole spectrum were acquired in list mode for both detector heads individually. The list mode data was processed as described in section 2.2.1, reformatted into conventional 128×128 pixels images.

The experimental and simulated images were scatter corrected as described in section 2.3.1. Using IDL the sum of counts over the entire image was calculated. The system planar sensitivity was calculated as,

$$S_{system} = \frac{\left(C_{tot} / t_{acq}\right)}{A_t}$$ Equation 2-15

where C_{tot} is the summed counts, t_{acq} is the acquisition time and A_t is the activity within the phantom at the time of acquisition. The mean of the system planar sensitivity for detector head one and two was taken as the camera sensitivity.

2.5.2 System spatial resolution

The sharpness of the images is limited by several factors, including intrinsic resolution, collimator resolution, electronic noise in the detection process, scattered radiation and septal penetration. The system spatial resolution (henceforth simply referred to as spatial resolution) can be estimated by means of the *Full Width at Half Maximum* (FWHM) of the profile from a line source of radiation projected by the collimator onto the detector. This profile is also called the *Line-Spread Function* (LSF) [6].

Figure 3 shows the line source and the stand that was used for the resolution measurements and simulations. The activity was enclosed in a 50 cm plastic tube with an inner diameter of 1 mm and a wall thickness of 1 mm. This tube was supported by a Perspex frame.

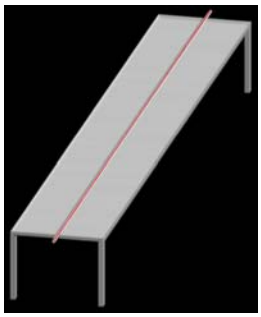

Figure 3. *The line source tube (red) supported with a stand to keep it straight.*

The line source was filled with an activity of 50 MBq ^{111}In chloride and placed at the centre of the crystal at a distance of 10 cm from the face of the collimator in both the X- and Y-direction. List mode acquisition was performed until 10 million counts were acquired for both

detector heads. The list mode data was processed as described in section 2.2.1 and reformatted into 256×256 pixel matrices with a pixel size of 2.3×2.3 mm^2.
The experimental and simulated images were read into IDL. The ten central rows in the image with the line source in the X-direction were put in to an array to which a Gaussian function was fitted. From this function the FWHM, given in rows, was obtained. By multiplying this value with the pixel size, a value of this FWHM with the unit length was obtained. The essential features of the IDL program can be seen in Appendix 2. The same procedure was carried out for the ten central rows in the image with the line source in the Y-direction. This was done for the two heads individually for all images. A mean value of the FWHM in the X- and Y-directions for both detector heads was taken as the resolution value.

2.5.3 Image contrast

For the image contrast measurements a heterogeneous phantom filled with activity to mimic the biodistribution in clinical data was used. Inside the large cylinder, made of Perspex, were three insert cylinders: one made of Teflon and two hollow ones made of Perspex. The hollow cylinders contained water and air respectively. The purpose of these insert cylinders was to resemble the spine, liver and lung respectively. Attached to the water filled cylinder was a smaller Perspex cylinder representing a tumour. The phantom is shown in Figure 4 and its dimensions are shown in Table 4. The volume, activity and activity concentrations of ^{111}In chloride in the phantom at the time of acquisition are shown in Table 5. As seen in Table 5, the tumour uptake for the antibody ^{111}In-DOTA-Tyr^3-octreotide is, compared to other radiopharmaceuticals, exceptional high.

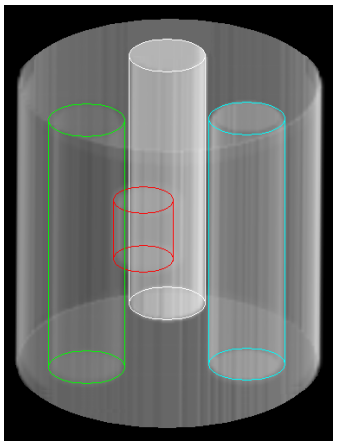

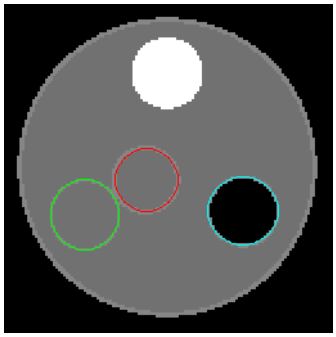

Figure 4 a. *The phantom used for the contrast measurements. The white, green, blue and red cylinders respresent the* ***b.*** *The transverse plane in the centre of the phantom.*

spine, liver, lung and tumour respectively.

Table 4. The measurements of the major phantom and inserts used for contrast measurements.

	Outside diameter (cm)	Inside diameter (cm)	Outside height (cm)	Inside height (cm)
Large cylinder	20.0	19.0	21.1	20.1
Air- and water inserts	4.8	4.2	18.7	18.3
Teflon insert	4.8	-	18.7	-
'Tumour'-insert	4.6	4.0	4.6	4.0

Table 5. Volume, activity and activity concentrations[1] of ^{111}In chloride in the major phantom with inserts at the time of acquisition.

	Volume (cm^3)	Activity (MBq)	Activity concentration (MBq/ml)	Activity concentration normalized to background
Background	4 554	36.3	8.0E-3	1
Liver	281	14.2	5.1E-2	6
Tumour	50	47.4	9.3E-1	116

[1] The data is taken from *'Biokinetics and dosimetry in patients administered with 111In-DOTA-Tyr3-octreotide: implications for internal radiotherapy with 90Y-DOTATOC'* by Marta Cremonesi et al.

In the experiments the phantom was placed on the patient table centred between the detectors. The two detector heads were positioned close to the phantom and couch in the anterior and posterior views respectively. Approximately 25 million counts per head were acquired in list mode. The list mode data was processed as described in section 2.2.1. The images were reformatted into conventional 128×128 pixels matrices with a pixel size of 4.7×4.7 mm^2.

The experimental and simulated images were scatter and attenuation corrected and transformed in to 'count rate images' as described in section 2.3.1 and 2.3.2 respectively. Thereafter the images were read in to *A Medical Image Data Examiner* (AMIDE) for *region of interest* (ROI) drawing. Four square ROI's with a size of 4×4 pixels were placed over the tumour, liver, spine and lung. The placements of the ROI's (in the experimental 171 keV image with no scatter correction) are showed in Figure 5.

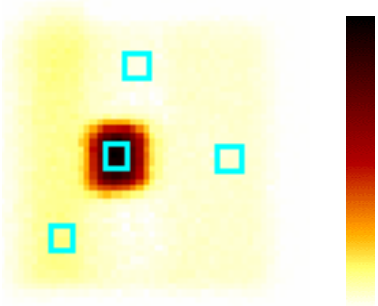

Figure 5. *Four ROI's placed over the 'tumour', 'liver', 'spine' and 'lung' on the experimental 171 keV image with no scatter correction.*

The contrast of the tumour to the liver, spine and lung was calculated as

$$c = \frac{(mean_{tumour} - mean_b)}{(mean_{tumour} + mean_b)} \qquad \text{Equation 2-16}$$

where $mean_{tumour}$ is the mean pixel value in the tumour-ROI and $mean_b$ is the mean pixel value in the liver-, spine- or lung-ROI.

2.5.4 Absolute signal level and activity quantification

For these measurements a water filled cylindrical Perspex phantom with a cylindrical insert filled with activity and placed in the centre was used. The phantom is shown in Figure 6 and the dimensions are shown in Table 6.

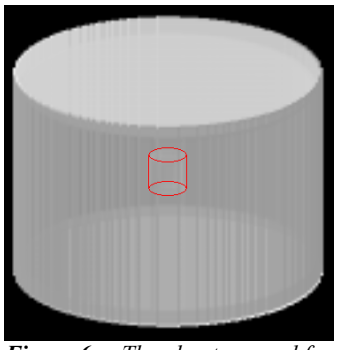

Figure 6 a. *The phantom used for the absolute signal level and activity quantification measurements.*

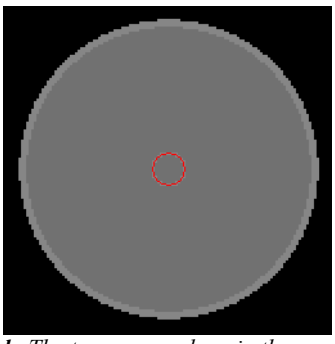

b. *The transverse plane in the centre of the phantom.*

Table 6. The measurements of the major and insert phantom used for sensitivity and partial volume effect measurements.

	Outside diameter (cm)	Inside diameter (cm)	Outside height (cm)	Inside height (cm)
Large cylinder	20.0	19.0	14.0	13.0
Insert	2.4	2.0	2.4	2.0

The insert was filled with an activity of 10 MBq ^{111}In chloride and placed in the centre of the water filled phantom. For the experiments the phantom was placed on the patient couch centred between the detectors. The two detector heads were positioned one centimetre from the phantom and the couch in the anterior and posterior views respectively. Approximately 3 million counts per head were acquired in list mode. The list mode data was processed as described in section 2.2.1. The images were reformatted into conventional 128×128 pixels matrices with a pixel size of 4.7×4.7 mm^2.

The experimental and simulated images were scatter and attenuation corrected and transformed in to 'count rate images' as described in section 2.3.1 and 2.3.2 respectively. Thereafter the images were read in to AMIDE for ROI drawing. The size of the ROI was the same as the actual size of the insert phantom, i.e. 2×2 cm^2. The placement of the ROI (in the experimental 171 keV image with no scatter correction) is showed in Figure 7.

Figure 7. *A ROI with the same size as the enclosed activity drawn on the experimental 171 keV image with no scatter correction.*

The number of *counts per second* (cps) from the ROI, $R_{0,ROI}$, was calculated as

$$R_{0,ROI} = mean_{ROI} \cdot p_{ROI} \qquad \text{Equation 2-17}$$

where $mean_{ROI}$ is the mean pixel value (counts per second) in the ROI and p is the number of pixels in the ROI. In the same way, the count rate for the whole image, $R_{0,all}$, was calculated as

$$R_{0,all} = mean_{all} \cdot p_{all} \qquad \text{Equation 2-18}$$

Where $mean_{all}$ is the mean pixel value in the whole image and p_{all} is the number of pixels in the whole image.

Ideally $R_{0,ROI}$ and $R_{0,all}$, would have the same numerical value, but as a result of scattered photons and the resolution of the camera the signal is distributed over a volume that is larger than the actual size of the source. The percentage of the photons that were 'spilled out' was calculated as

$$spill - out = \frac{R_{0,ROI}}{R_{0,all}} \cdot 100 \qquad \text{Equation 2-19}$$

The number of counts per second per MBq (*absolute signal level*) originating from the ROI, S_{ROI}, and the whole image, S_{all}, were calculated as

$$S_{ROI} = \frac{R_{0,ROI}}{A_t} \qquad \text{Equation 2-20}$$

$$S_{all} = \frac{R_{0,all}}{A_t} \qquad \text{Equation 2-21}$$

where A_t is the true activity enclosed in the insert at the time the images were taken. Converse, given that the camera sensitivity, S_{system}, was known, the activity in the ROI, A_{ROI}, was calculated as

$$A_{ROI} = \frac{R_{0,ROI}}{S_{system}} \qquad \text{Equation 2-22}$$

and the activity in the whole image, A_{all}, was calculated as

$$A_{all} = \frac{R_{0,all}}{S_{system}} \qquad \text{Equation 2-23}$$

The *absolute signal level* (Equations 2-20 and 2-21) is strictly speaking a measurement of the sensitivity. However, separate terms have been used owing to the fact that *sensitivity* is strongly associated with the definition according to NEMA standard (*National Electrical Manufacturer Association*), saying that a sum over the entire image of a flat plastic dish should be used in the calculations (Equation 2-15).

2.6 Error calculations.

In order to calculate the error of the results achieved in this study the *error propagation formula* was used. If x and y are directly measured variables for which σ_x and σ_y are known, the standard deviation for any quantity u derived from these can be calculated by

$$\sigma_u^2 = \left(\frac{\partial u}{\partial x}\right)^2 \cdot \sigma_x^2 + \left(\frac{\partial u}{\partial y}\right)^2 \cdot \sigma_y^2 + \ldots \qquad \text{Equation 2-24}$$

where $u = u(x, y)$ represents the derived quantity. The errors for the experimental data were estimated based on the directly measured numbers of counts in the images, the accuracy of the source activity given by the manufacturer and the accuracy of the balance used in the preparations. The errors for the simulated data were based solely on the numbers of counts in the images.

3. Results and discussion

In this section the results and associated errors are presented. For all charts a corresponding table of results can be found in Appendix 3.

3.1 System planar sensitivity

Figure 8 shows the values of the sensitivity calculated as described in section 2.5.1 for the ten different window settings. These values were used for the activity quantification described in section 2.5.4.

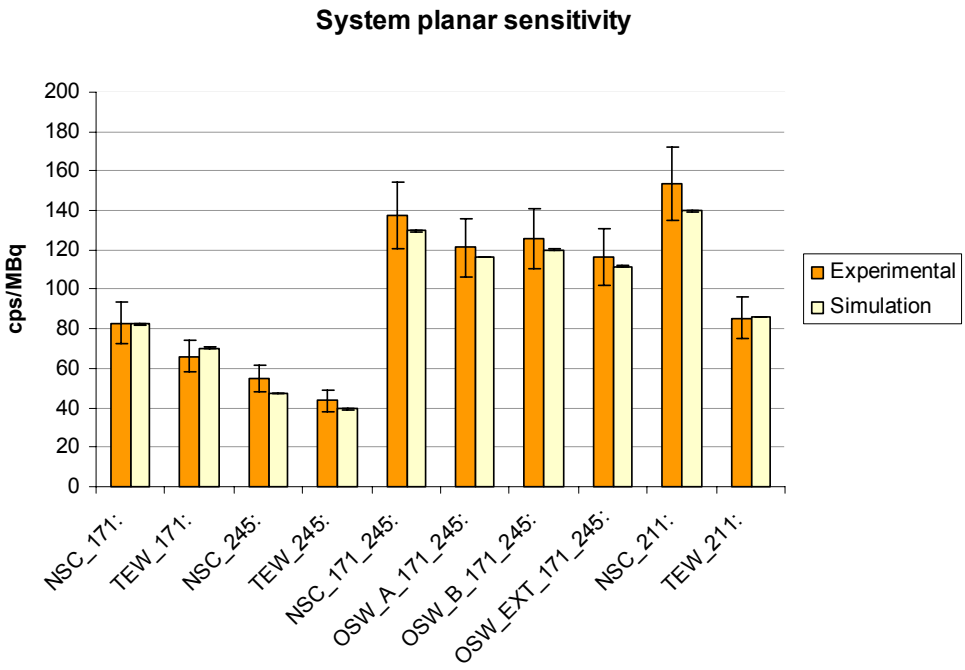

***Figure 8**. Calculated values of the system planar sensitivity for the ten different window settings.*

The experimental and simulated data are in good agreement and are within the calculated errors associated with the values. It can be seen that the scatter corrected images have a lower sensitivity than the uncorrected ones, as would be expected since events have been subtracted. It can also be seen that using both photopeaks give rise to a higher sensitivity value compared to that using only one. The sensitivity in terms of absolute signal level is further discussed in section 3.4.

3.2 System spatial resolution

Figure 9 shows the spatial resolution calculated as described in section 2.5.2. Since the measurements were performed without scatter material little difference is seen between the different window settings. The experimental values vary from 1.1-1.2 cm and all simulated values are 1.0 cm. The disagreement between the experimental and simulation results may be an indication that the intrinsic spatial resolution value used as input in SIMIND in fact is too small (3.12 mm at 140 keV for the central field of view). This value is taken from the acceptance test performed in the year 2000. It is quite possible that the resolution has degraded since then due to ageing of the components in the camera. This could be tested by again measuring the resolution according to the NEMA standard. Too low a value of the intrinsic energy resolution in the simulations would also make a contribution to this effect; this is further discussed in section 3.5 (spectrum evaluation).

Figure 9 shows no estimated errors due to the fact that the errors connected with the function *Gaussfit* used in IDL are unknown. However, the statistics in the profiles were high and the errors are probably smaller than the pixel size.

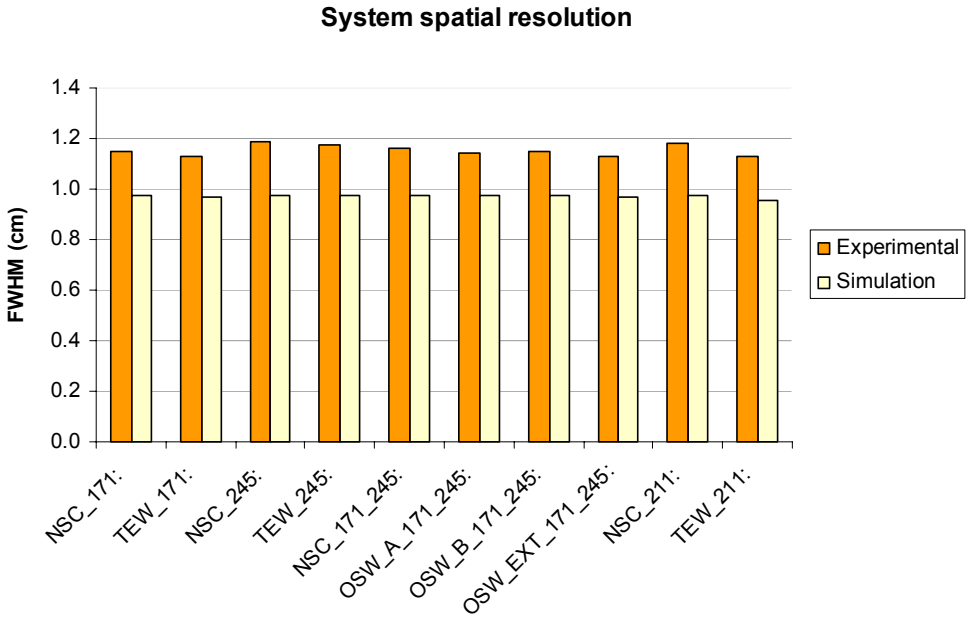

***Figure 9**. Calculated values of the system spatial resolution.*

3.3 Image contrast

Figure 10 shows the contrast values of the 'tumour' relative to the 'lung', calculated as described in section 2.5.3. The results were similar for the contrast relative to the 'liver' and 'spine' (see Appendix 3).

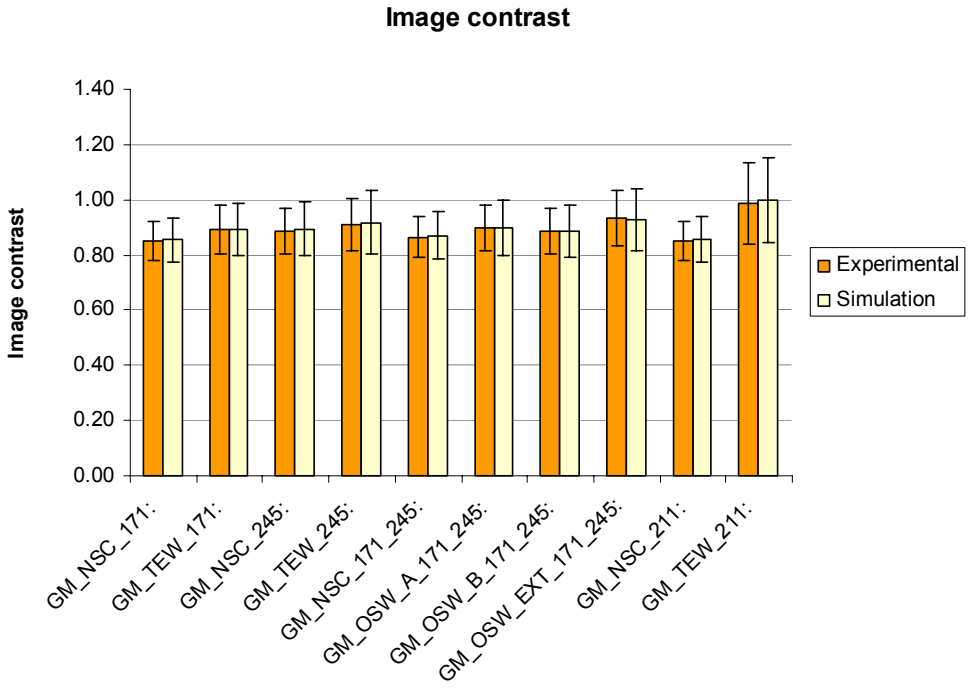

***Figure 10**. Calculated contrast values of the 'tumour' relative to the 'lung'. The prefix GM indicates that the images have been attenuation corrected using the geometrical mean method.*

The experimental and simulation data is agreeable, differing by 1 % at the most. The chart shows that the differences in the image contrast between the window settings are within errors, although a tendency that scatter correction improves the image contrast can be seen. The lowest image contrast is obtained when using window setting NSC_171 and NSC_211, due to the higher fraction of scattered events. The highest image contrast when using both photopeaks is obtained with window settings OSW_EXT_171_245 and TEW_211 (see also visual evaluation in section 3.6).

3.4 Absolute signal level and activity quantification

Figures 11 and 12 show the values of the *Absolute Signal Level* (ASL) from the ROI and from the whole image respectively, calculated as described in section 2.5.4. The amount of spill out in the images is shown in Figure 13. Calculated values of the activity within the insert based on the ROI and the whole image are shown in Figures 14 and 15 respectively. The green column in the figures represents the true activity in the insert.

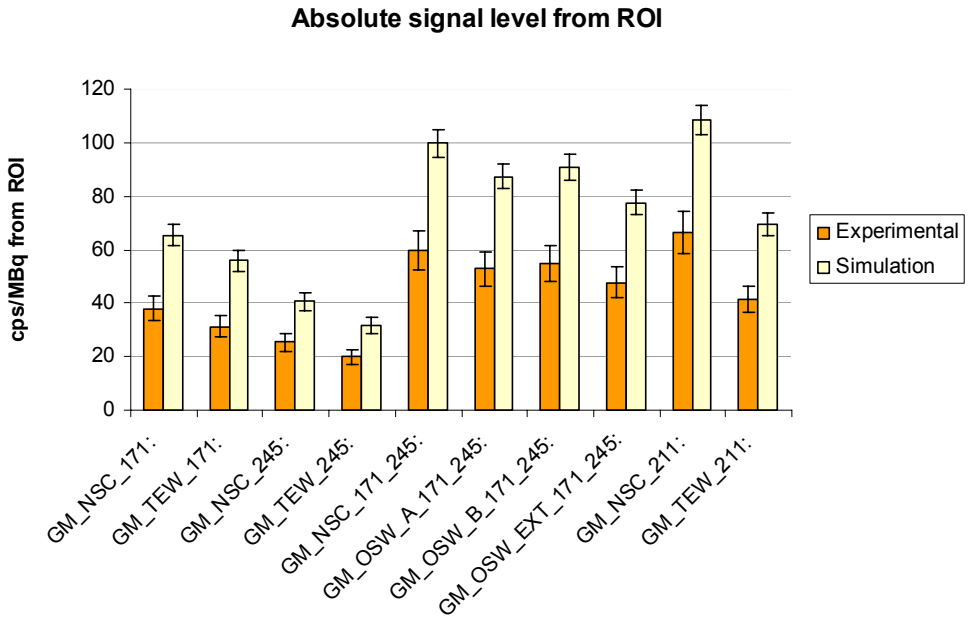

Figure 11. *The absolute signal level from the ROI.*

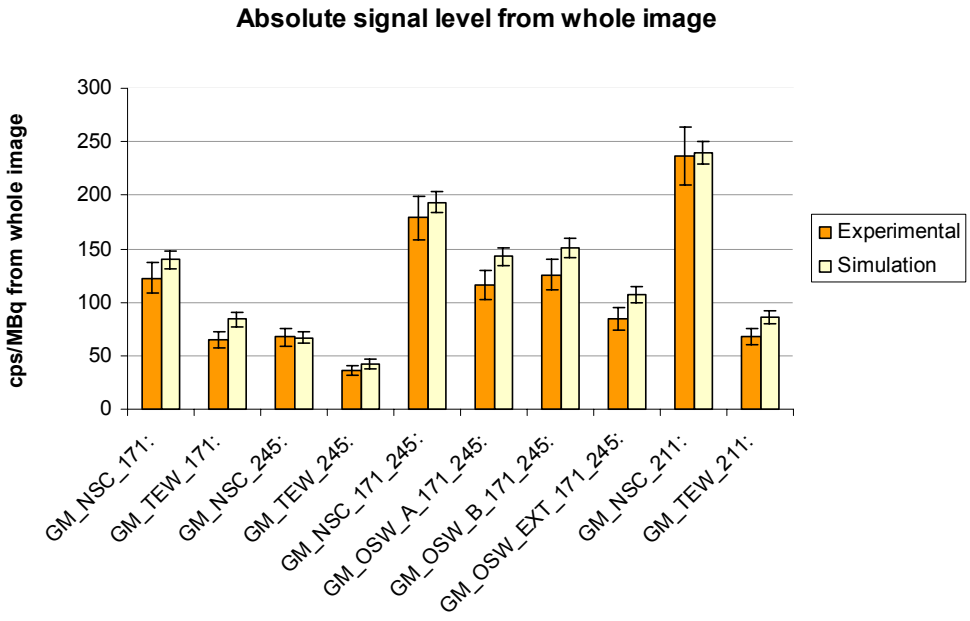

Figure 12. *The absolute signal level from the whole image.*

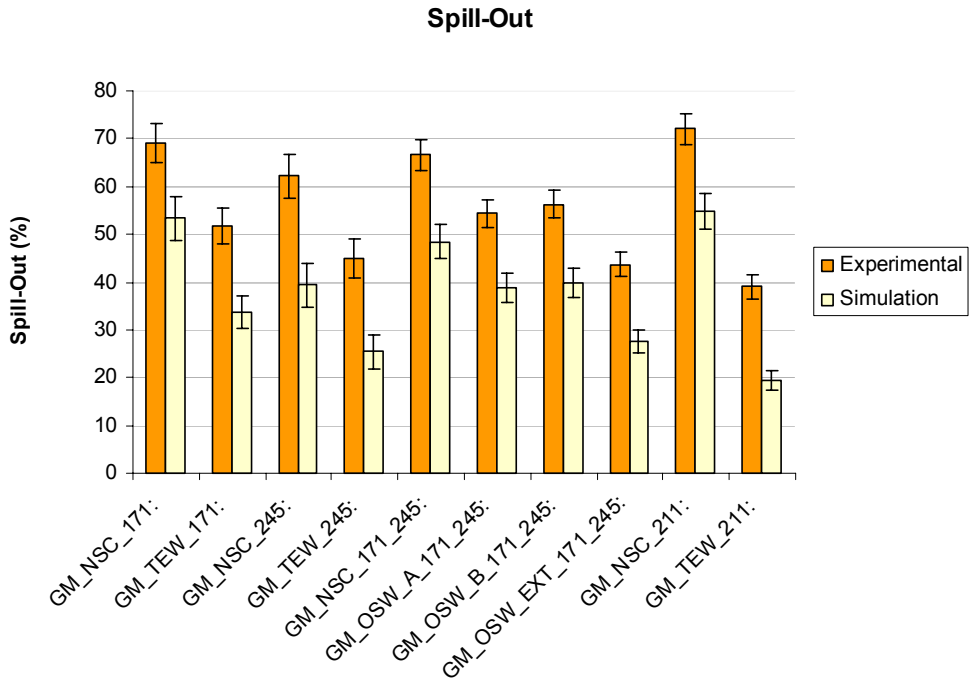

***Figure 13**. Calculated 'spill out' from the ROI to the surroundings.*

The level of agreement between experimental and simulation ASL values is significantly better when based on the whole image than when based on the ROI. This is elucidated in Figure 13, showing that there is more spill out in the experimental images than in the simulated ones. This disagreement further indicates that the resolution values (intrinsic spatial and intrinsic energy resolution) used in the simulations in fact is too low.

Nevertheless, the same trends are seen in the ASL values in both the experiments and simulations. The figures show, as mentioned earlier for the system camera sensitivity, that the scatter corrected images have a lower ASL than the uncorrected ones and that using both photopeaks gives rise to higher ASL values compared to using only one. From a clinical imaging point of view a high ASL is desirable in order to lower the acquisition time for the patient and/or in order to increase the *Signal to Noise Ratio* (SNR). When comparing the window settings, which comprise scatter correction, the OSW-window settings give rise to the highest ASL.

In Figure 13 it can be seen that 'spill out' is more evident in the images without scatter correction, which basically indicates that the scatter in the images principally end up in the surroundings of the source.

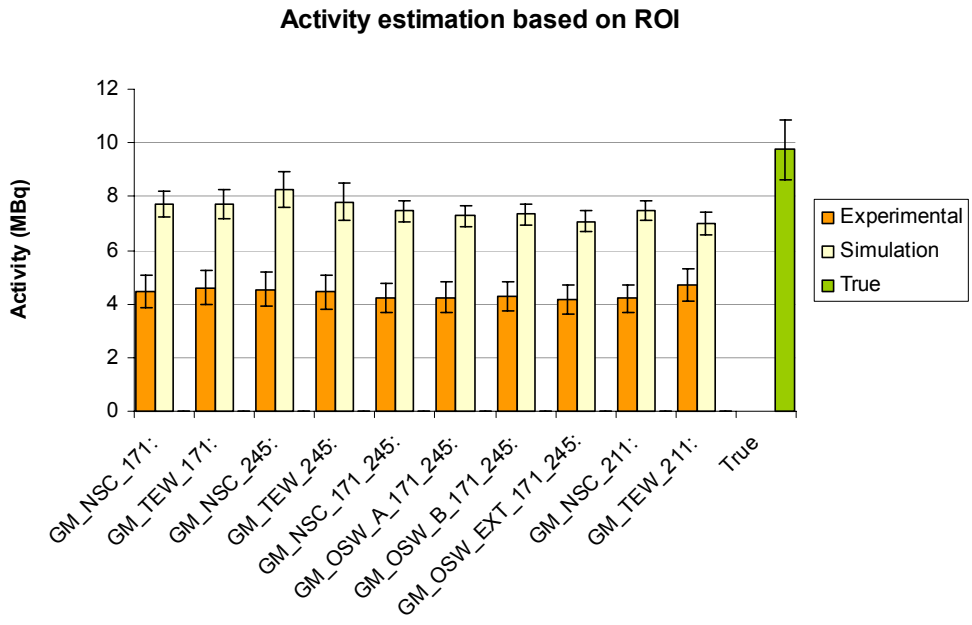

Figure 14. *Calculated values of the activity in the source based on the ROI the same size as the source. The green column represents the true activity in the source.*

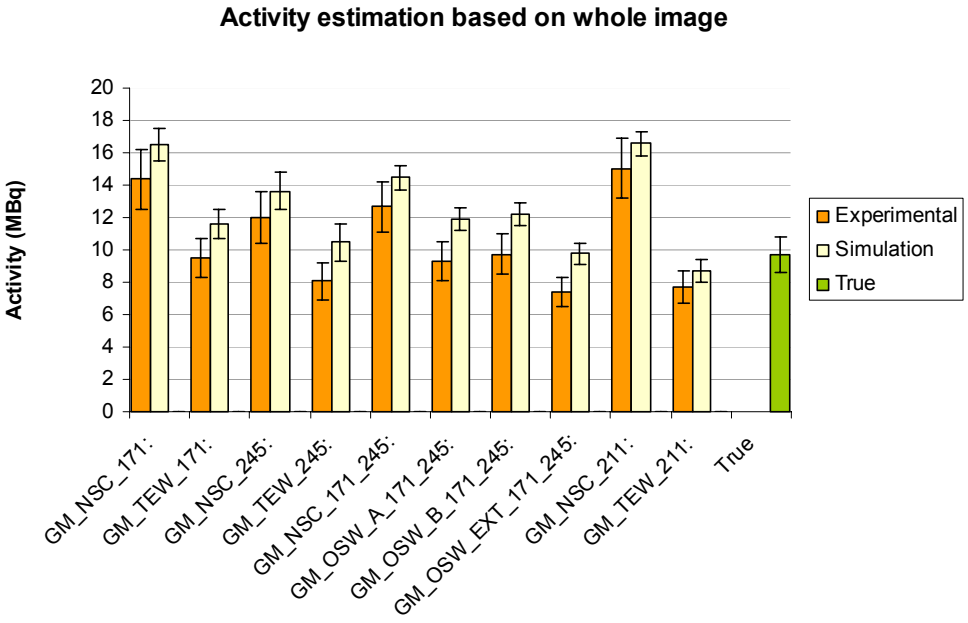

Figure 15. *Calculated values of the activity in the source based on the whole image. The green column represents the true activity in the source.*

Activity quantification based on the ROI leads to an underestimation of the activity for all window settings, as a result of spill out. Figure 14 also indicates, as stated before, that there is more spill out, and therefore more loss in activity in the ROI, in the experimental images. The activity quantification is more accurate when based on the whole image, as shown in Figure 15. From this figure it is evident that images that are not scatter corrected give rise to an overestimate of the activity. The scatter corrected images give rise to more accurate activity quantification.

3.5 Spectrum evaluation

Since the experimental acquisitions were performed in list mode, spectrum files could be created. Spectra were also obtained in the simulations. Figure 16 (a) shows the spectra from experiments and simulations of the simple water filled phantom with an active insert (shown in Figure 6). The black line represents all detected photons in the simulation and the red line illustrates the detected photons that have been scattered at least once. The blue line represents the experimental spectrum. In Figure (b) the primary photons and the photons that have been scattered one, two or three times etc. (labelled SC) have been separated.

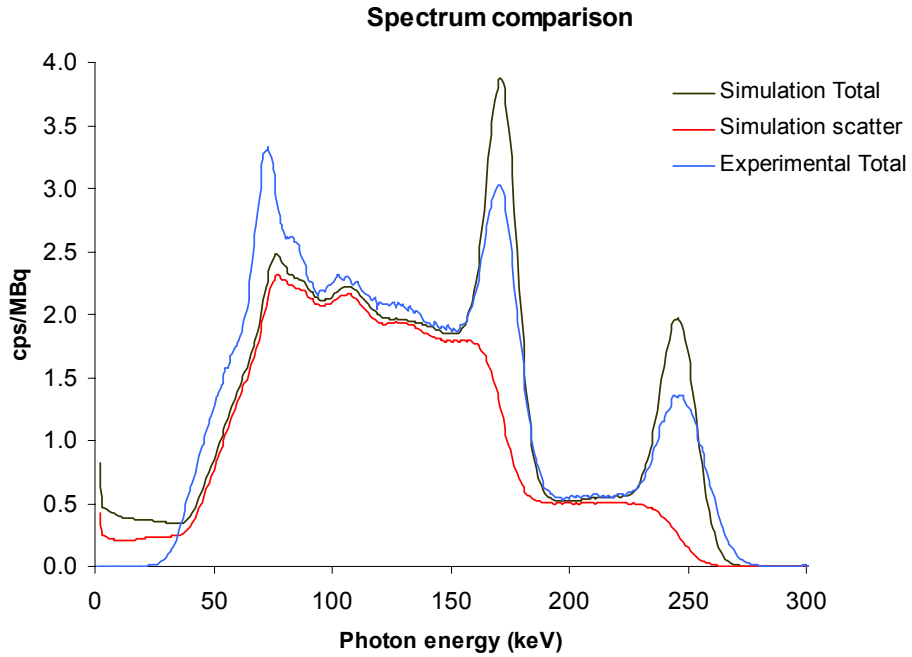

Figure 16 (a). *The spectrum from the experiment (blue) and simulation (black) of the water filled cylinder with an active insert in the centre. The red line represents the detected scattered photons in the simulation.*

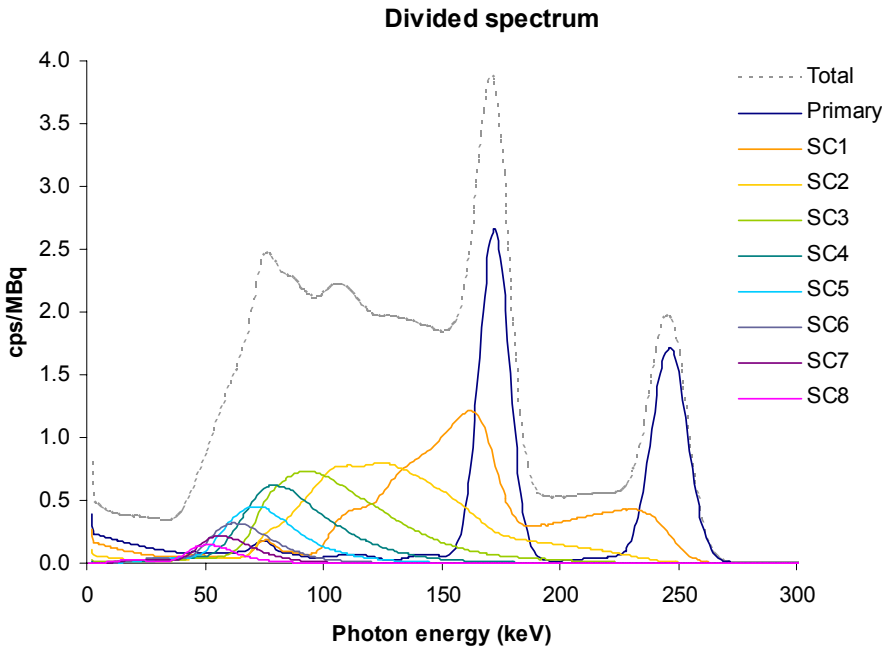

(b). *The simulation spectrum divided in to primary and scattered (SC) events.*

In Figure 16 a good accordance between the experimental and simulated spectrum is seen apart from the regions of the photopeaks and the characteristic x-ray peak (at 70-80 keV). The sensitivity is higher in the regions of the photopeaks in the simulated spectra than in the experimental one. This is consistent with the *absolute signal level* shown in Figure 12, where the simulated values are consistently slightly higher than the experimental. It can also be seen that the characteristic x-ray peak is more apparent in the experimental spectrum. This can be explained by the fact that there is surrounding scattering material in the camera room and that SIMIND is a model of the camera in vacuum. In the experiments there are two detector heads facing each other which makes it possible for them to detect scattered photons and characteristic x-rays originating from the opposite detector and collimator. However, this has no effect on the results in this study seeing that it does not interfere with the energy windows of interest.

Figure 17 (a)-(f) shows illustrations of the scatter corrections connected with the different window settings where the yellow areas denote the events deleted after scatter correction. The calculated experimental *Scatter to Total* (S/T) values for these window settings are shown in Table 7 together with the values obtained from simulations, which are assumed to be 'true'. The NSC window settings are not shown since no scatter corrections are applied with them.

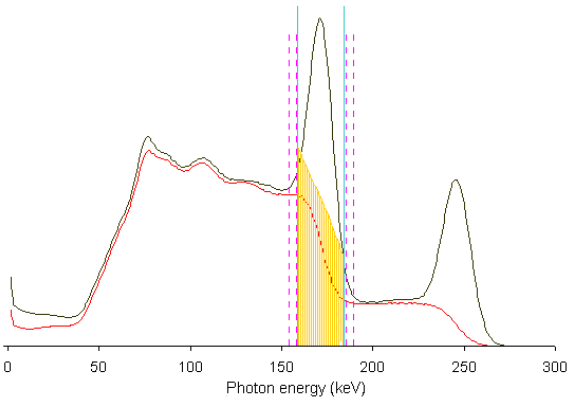

Figure 17 (a). *TEW_171.*

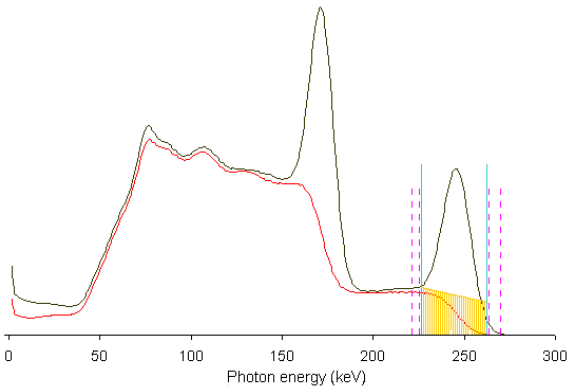

(b). *TEW_245.*

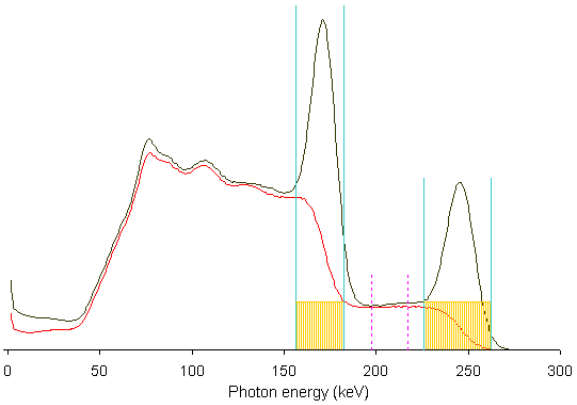

(c). *OSW_A_171_245.*

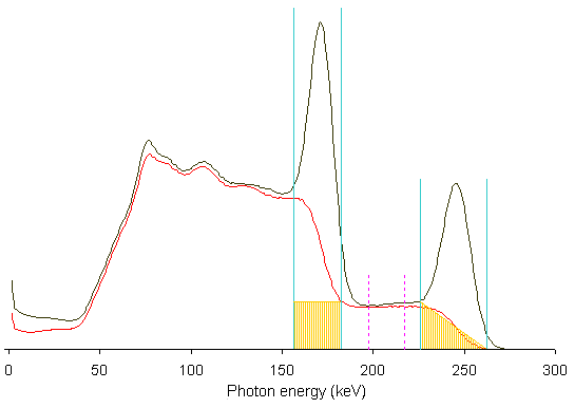

(d). *OSW_B_171_245.*

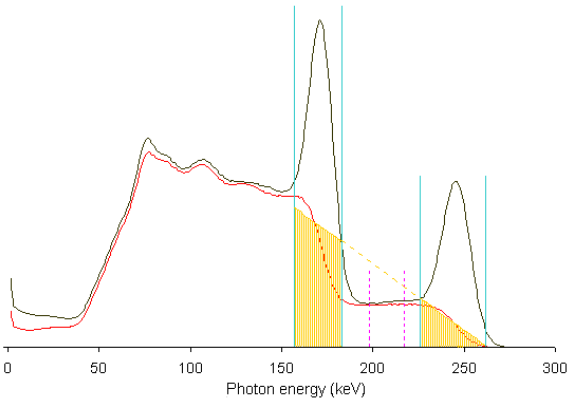

(e). *OSW_EXT_171_245.*

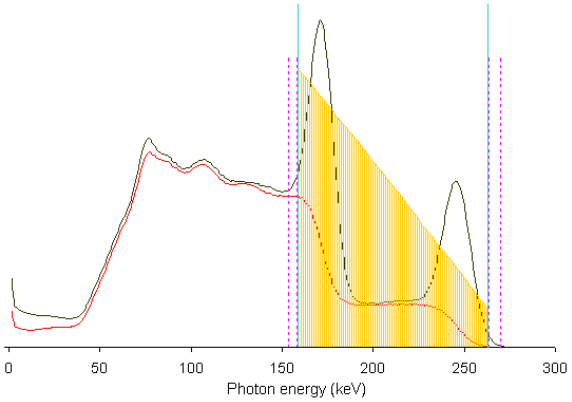

(f). *TEW_211.*

Table 7. Calculated S/T values from the experimental data and true S/T values obtained from simulations.

	Scatter to total ratio		
Window setting	*Experimental*	*Simulation*	
TEW_171:	0.40	0.43	(-7%)
TEW_245:	0.38	0.22	(+73%)
OSW_A_171_245			
171 keV window:	0.26	0.43	(-67%)
245 keV window:	0.37	0.22	(+67%)
OSW_B_171_245			
171 keV window:	0.26	0.43	(-67%)
245 keV window:	0.25	0.22	(+10%)
OSW_EXT_171_245			
171 keV window:	0.51	0.43	(+16%)
245 keV window:	0.25	0.22	(+10%)
TEW_211:	0.62	0.44	(+41%)

The values in parentheses are the percentage over-/underestimation of scatter when the S/T values from the simulations are assumed to be true.

When only taking the S/T values into consideration, window setting TEW_171 exhibit the best scatter estimation with an underestimation of 7 %. Window settings TEW_245 and TEW_211 exhibit the most significant overestimation of scatter by 73 % and 41 % respectively. Window setting OSW_A_171_245 underestimates the scatter in the 171 keV window and overestimates it in the 245 keV window by 67 %. Window settings OSW_B_171_245 has the same underestimation in the 171 keV window but shows a better agreement in the 245 keV window with an overestimation of 10 %. The best agreement, when using both photopeaks, is obtained with window setting OSW_EXT_171_245, which has an overestimation by 16 % and 10 % in the 171 keV and 245 keV windows respectively.

3.6 Visual evaluation

Figures 18-23 demonstrates how well the deleted scatter images from the different window settings correspond to the true scatter for the heterogeneous phantom. All images shown are from simulations. The experimental images are in good accordance with the simulated ones (see Appendix 4). Figure 18 shows the ‘air’ images when using one main energy window, which, as mentioned earlier, represent the ideal image to achieve after scatter and attenuation correction has been applied to the ‘total’ images. Since the ideal image and the true scatter change with the placement of the main window there are four sets of images, derived from:

15 % energy window centred at 171 keV, 15 % energy window centred at 245 keV, 50 % energy window centred at 211 keV and two 15 % energy windows centred at 171 and 245 keV. Figures 19 and 20 show the true scatter and the images without scatter correction respectively when using one main energy window. Figure 21 shows the TEW scatter corrected images and Figure 22 shows the scatter images deleted. Figure 23 shows the corresponding images for the OSW window settings. Since these ones comprise scatter correction of both the 171 keV and 245 keV images the 'true' scatter has been divided in to two images.

The band of activity across the images is a result of the differing activity concentrations and atomic number within the inserts of the phantom, see Figure 4.

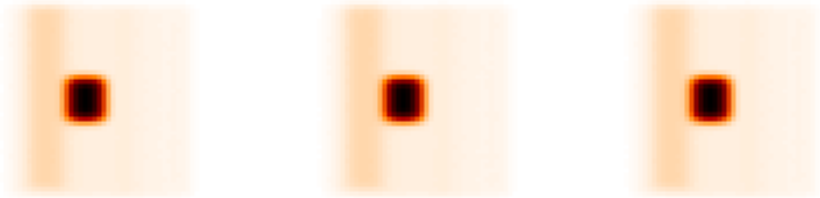

***(a)**. 171 keV 15%* ***(b)**. 245 keV 15%* ***(c)**. 211 keV 50%*

***Figure 18**. The ideal images when using one main energy window.*

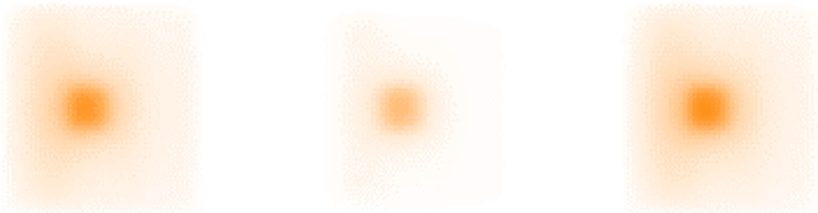

***(a)**. 171 keV 15%* ***(b)**. 245 keV 15%* ***(c)**. 211 keV 50%*

***Figure 19**. The real scatter images when using one main energy window.*

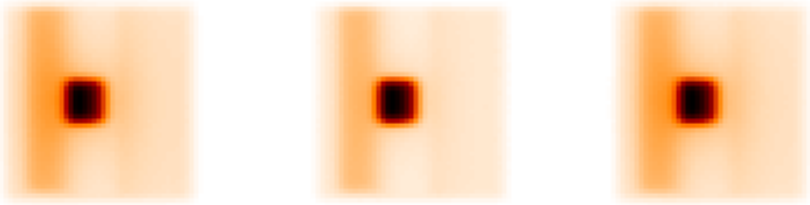

***(a)**. GM_NSC_171* ***(b)**. GM_NSC_245* ***(c)**. GM_NSC_211.*

***Figure 20**. The attenuation corrected images using one main energy window before scatter correction (GM denotes Geometrical Mean attenuation correction).*

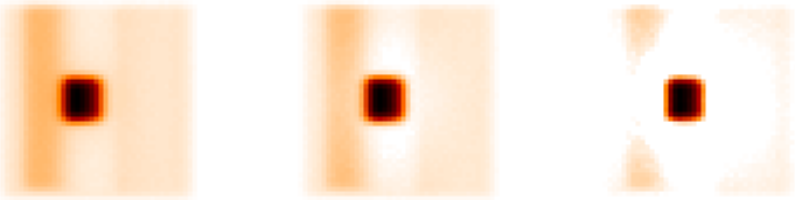

***(a)**. GM_TEW_171* ***(b)**. GM_TEW_245* ***(c)**. GM_TEW_211*

***Figure 21**. The attenuation- and TEW scatter corrected images.*

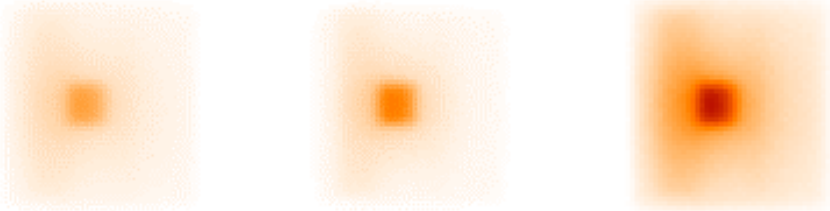

***(a).** TEW_171* ***(b).** TEW_245* ***(c).** TEW_211*

***Figure 22**. The scatter images deleted when using one main energy window and TEW scatter correction.*

***(a)**. 171 and 245 keV 15% , ideal image*

***(b)**. Real scatter contribution from the 171 keV window*

***(c)**. Real scatter contribution from the 245 keV window*

***(d)**. GM_NSC_171_245, attenuation corrected image before scatter correction*

***(e)**.**GM_**OSW_A_171_245, attenuation- and scatter corrected image*

***(f)**. GM_OSW_A_171_245, scatter image deleted from the 171 keV image*

***(g)**. GM_OSW_A_171_245, scatter image deleted from the 245 keV image*

***(h)**. GM_OSW_B_171_245, attenuation- and scatter corrected image*

***(i)**. GM_OSW_B_171_245, scatter image deleted from the 171 keV image*

***(j)**. GM_OSW_B_171_245, scatter image deleted from the 245 keV image*

***(k)**. GM_OSW_EXT_171_245, scatter corrected*

***(l)**. GM_OSW_EXT_171_245, scatter image deleted from the 171 keV image*

***(m)**. GM_OSW_EXT_171_245, scatter image deleted from the 245 keV image*

***Figure23.** The ideal image and true scatter compared to the images obtained with the OSW window settings with corresponding correction methods.*

From the images it becomes evident that when using window setting TEW_211 and TEW_245 too many events are deleted, as indicated by the S/T values in Table 7. In Figure 21 it can be seen that these two window settings lead to deletion of primary photons in the 'tumour' and its surroundings. The scatter image deleted with window setting TEW_171

agree quite well with the true scatter apart from a slight underestimation of scatter events in the region of the 'tumour'. The three OSW window settings all base their scatter estimation on the scatter window centred between the two photopeaks. The difference between them is the fraction deleted and the distribution between the two photopeaks. It can be seen both in the images and in the S/T values that; window setting OSW_A_171_245 underestimates the scatter in the 171 keV image and overestimates it in the 245 keV image; window setting OSW_B_171_245 underestimates the scatter in the 171 keV image but has a quite good agreement in the 245 keV image; window setting OSW_EXT_171_245 exhibits a scatter estimation that is in quite good accordance for both images.

Figure 24 (a)-(d) shows plotted profiles over the images of the heterogeneous phantom in order to see how well the objects are resolved in the processed images for the different window settings. The black profiles come from the 'ideal' images from the different windows.

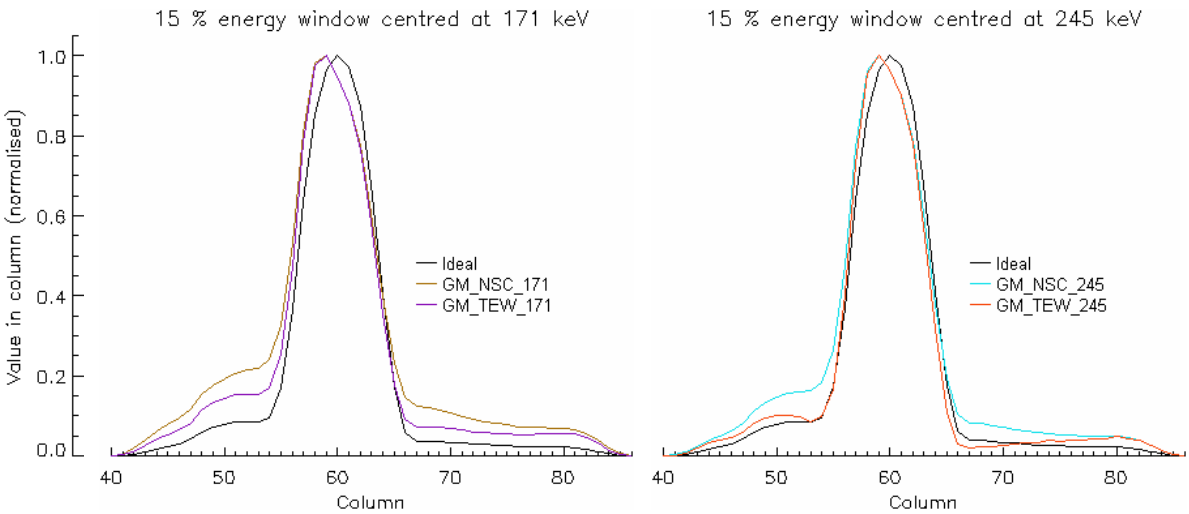

***Figure 24 (a)**. Profiles over the images created with the window settings NSC_171 and TEW_171.GM denotes that the image has been attenuation corrected.*

***(b)**. Profiles over the images created with the window settings NSC_245 and TEW_245.*

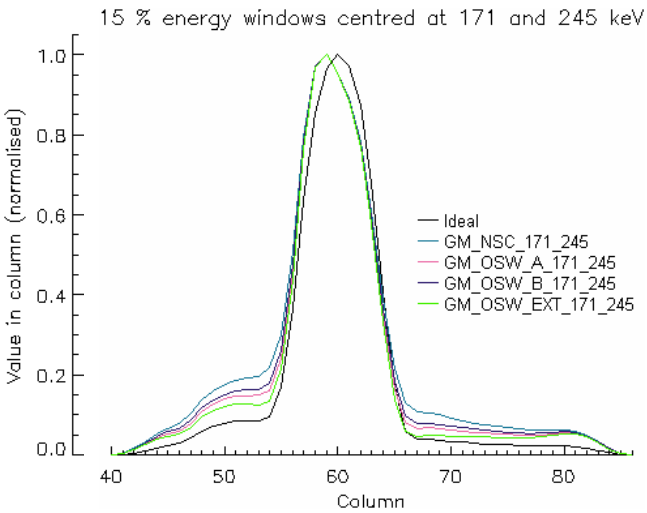

***(c)**. Profiles over the images created with the window settings NSC_171_245, OSW_A_171_245, OSW_B_171_245 and OSW_EXT_171_245.*

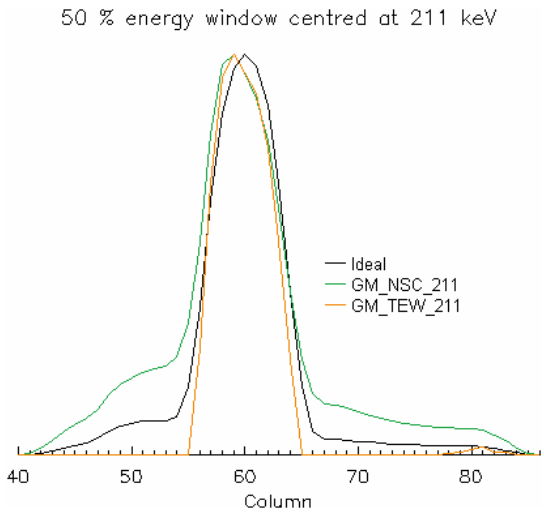

***(d)**. Profiles over the images created with the window settings NSC_211 and TEW_211.*

In Figure 16 it becomes apparent that the agreement between experimental and ideal profiles is worse in the images without scatter correction compared to the corrected ones. The window settings that are in the best agreement with the corresponding ideal profile are TEW_245 and OSW_EXT_171_245. Window setting TEW_211 demonstrates the least agreement with the ideal profile, seeing that almost all structures apart from the 'tumour' are lost.

3.7 General discussion

Generally, there was a satisfactory agreement between the outcomes of the experimental measurements and the simulations. However, there are a number of factors that could have contributed to the slightly differing results in the experiments and the simulations. For example, the septal penetration effect was not included in the simulations. This can be done but is relatively time consuming. Another reason could be that the energy resolution of the detector is modelled from an on-line convolution of the imparted energy by an energy-dependent Gaussian function that varies with $1/\sqrt{E}$. The simulation of the intrinsic spatial resolution of the crystal is based on the same idea [13]. However, it has been suggested in the literature that this energy-dependent function in fact is more complicated due to electrical noise, fluctuations and statistical variations in the processes taking place in the scintillation detector [6, 15]. One other possible contribution is the fact that SIMIND is a model of a system in vacuum, where scattering surroundings such as the floor and couch are absent.

However, a more pronounced difference is seen when comparing spill out in the experimental and simulated images. As mentioned earlier, this could be a result of using too low an

intrinsic energy- and spatial resolution value in SIMIND. These two parameters are interconnected: a low value of the energy resolution entails a lower value of the spatial resolution, hence causing less spill out, which is seen in the simulated images.

The background signal level for the scintillation camera was measured in list mode and was shown to be small compared to the signal level in the experiments (typically less than 3 %).

One parameter that has not been investigated in this study is the *Signal to Noise Ratio* (SNR). A potential problem with using narrow scatter windows is the fact that the low number of counts in the window will give a large error in the noise level, adding noise to the final image when subtracted. However, too wide a scatter window leads to an inaccurate estimate of scatter in the main window. Investigation of the optimal scatter window width with regards to SNR is outside of the scope of this project, but would be an interesting subject for future work.

Where scatter in the image is overestimated, such as in the window settings TEW_245 and TEW_211, subtraction leads to significant numbers of negative pixel values, which are all then set to zero. Another area of future work would be to investigate the effect of these negative values on parameters such as image contrast and sensitivity.

Attenuation correction was not a significant factor in this work, however if these techniques were to be applied clinically careful thought would have to be given to attenuation correction methods.

For all window settings systematic underestimates of the absolute activity were obtained (see Figure 14). This is due to the finite spatial resolution leading to significant *Partial Volume Effects*. When comparing different window settings in this project, the same sized object was used throughout. This means that the intercomparisons are not affected by partial volume. When quantifying activity in arbitrary sized objects this should be taken into consideration.

4. Conclusions

In Table 8 shown below the evaluated parameters are summarized. For every parameter, the results for the different window settings are compared relatively to each other and shown in colour codes. Red indicates a relatively inferior, yellow an intermediate and green a relatively good outcome. White indicates inseparability between the results.

Table 8. A summary of the parameters evaluated in this study.

Parameter \ *Window setting*	NSC_171	TEW_171	NSC_245	TEW_245	NSC_171_245	OSW_A_171_245	OSW_B_171_245	OSW_EXT_171_245	NSC_211	TEW_211
System spatial resolution	-	-	-	-	-	-	-	-	-	-
Image contrast										
Absolute signal level ROI										
Absolute signal level whole image										
Spill out										
Activity quantification ROI	-	-	-	-	-	-	-	-	-	-
Activity quantification whole image										
Scatter to total ratio										
Profile agreement										

Considering all of the parameters that have been examined, three of the window settings have a clear advantage over the others, namely OSW_A_171_245, OSW_B_171_245 and OSW_EXT_171_245. The three windows show very similar overall performance. The last window setting OSW_EXT_171_245 shows a slightly better agreement between measured and modelled scatter to total ratios and less spill out. The other two (OSW_A_171_245 and OSW_B_171_245) show slightly superior activity quantification. The ultimate choice between these three window settings would depend upon the final application.

5. Acknowledgements

First of all, I would like to thank my supervisors; Glenn Flux for helpful advise that made me think twice about everything I did and Michael Ljungberg for always being there when needed despite being 626.83 miles away. I would like to say a special thank you to my primary supervisor, Cecilia Hindorf, for excellent guidance, tremendous support and for having the patience of a Saint.

I would also like to thank a bunch of people at The Royal Marsden for helping me with various matters, making it possible to carry out this project. I want to thank Will Ryder for being a great problem solver and for getting the momentous machinery to work; Sarah Chittenden for always being willing to help and for staying with me to do measurements after dark; Carlotte Barker for supporting throughout and for consistently correcting my English; Sarah Heard for being a tremendous help in my data processing; Jonathan Gear for always answering my questions and helping me with wording, and last but definitely not least, Mike Partridge for excellent proofreading and for always putting things in perspective.

Thank you everybody else who has provided me with material and with who I have had rewarding discussions, all included.

6. References

[1] Hindorf, C., *'Internal Dosimetry – Macroscopic, Small-Scale and Microscopic Perspectives'*, PhD Thesis Department of Medical Radiation Physics, Lund University (2004)

[2] Loevinger R. et al., *'MIRD Primer for Absorbed Dose Calculations'*, **The Society of Nuclear Medicine, Inc.** (1991)

[3] Furhang E. et al., *'A Monte Carlo approach to patient-specifiv dosimetry'*, **Medical Physics** (1996) 23(9): 1523-1529

[4] Wernick M. et al., *'Emission Tomography – The Fundamentals of PET and SPECT'*, **Elsevier Inc.** (2004), ISBN: 0-12-744482-3

[5] Knoll G., *'Radiation Detection and Measurement'*, 3rd edition, **John Wiley & Sons, Inc.** (2000), ISBN: 0-471-07-07338-5

[6] Cherry S. et al., *'Physics in Nuclear Medicine'*, 3rd edition, **Saunders** (2003), ISBN: 0-7216-8341-X

[7] Gustafsson A. et al., *'Dual-window scatter correction and energy window setting in cerebral blood flow SPECT: a Monte Carlo study'*, **Physics in Medicine and Biology** (2000) 45: 3431-3440

[8] Förster G. et al., *'Preliminary data on biodistribution and dosimetry for therapy planning of somatostatin receptor positive tumours: comparison of ^{86}-DOTATOC and ^{111}In-DTPA-octreotide'*, **European Journal of Nuclear Medicine** (2001), 28: 1743-1750

[9] *'ENSF Decay Data in the MIRD Format for ^{111}In'*, **NNDC Brookhaven National Laboratory**, Database version of December 21, 2005 *(http://www.nndc.bnl.gov/mird/)*

[10] Bushberg J. et al., *'The Essential Physics of Medical Imaging'*, 2nd edition, **Lippincott Williams & Wilkins** (2002), ISBN: 0-683-30118-7

[11] Mah E., *'Evaluation of a Triple Energy Window Scatter Correction Method for SPECT Imaging'*, (*http://home.netcom.com/~eugenem/TEW.html*)

[12] Ljungberg M. et al., *'Monte Carlo Calculations in Nuclear Medicine – Applications in Diagnostic Imaging'*, **Institute of Physics Publishing Ltd** (1998), ISBN: 0-7503-0479-0

[13] Ljungberg M., *'The SIMIND Monte Carlo program Home Page'*, (*http://www.radfys.lu.se/simind/*)

[14] *'NEMA Standard Publication NU 1-2001 – Performance Measurements of Scintillation Cameras'*, **National Electrical Manufacturers Association** (2001)

[15] Itadzu H. et al.,*'Evaluation of Response Functions of 16"×16"×4" Large-sized NaI Scintillation Detector for Environmental Gamma-ray Survey'*, (*http://ccwww.kek.jp/kek/rad/egs4/itadzu.pdf*)

[16] Carrasquillo J. A. et al., *'Similarities and Differences in ^{111}In- and ^{90}Y-Labeled 1B4M-DTPA AntiTac Monoclonal Antibody Distribution'*, **Journal of Nuclear Medicine** (1999) 40: 268-276

[17] Lövqvist A. et al., *'PET Imaging of ^{86}Y-Labeled Anti-Lewis Y Monoclonal Antibodies in a Nude Mouse Model: Comparison Between ^{86}Y and ^{111}In Radiolabels'*, **Journal of Nuclear Medicine** (2001) 42: 1281-1287

[18] Onthank D. C. et al., *'90Y and 111In Complexes of a DOTA-Conjugated Integrin $\alpha_v\beta_3$ Receptor Antagonist: Different but Biologically Equivalent'*, **Bioconjugate Chemistry** (2004) 15: 235-241

Appendix 1

Processing program for scatter and attenuation correction

```
PRO Process_program

                                                    The images created in list mode are opened
OpenR,1, '/home/raw_images/H1_171_15.img'           15% window centred at 171 keV, head 1
OpenR,2, '/home/raw_images/H1_155_2.img'            2% window centred at 155 keV, head 1
OpenR,3, '/home/raw_images/H1_187_2.img'            2% window centred at 187 keV, head 1
OpenR,4, '/home/raw_images/H2_171_15.img'           15% window centred at 171 keV, head 2
OpenR,5, '/home/raw_images/H2_155_2.img'            2% window centred at 155 keV, head 2
OpenR,6, '/home/raw_images/H2_187_2.img'            2% window centred at 187 keV, head 2
OpenR,7, '/home/raw_images/H1_245_15.img'           15% window centred at 245 keV, head 1
OpenR,8, '/home/raw_images/H1_224_2.img'            2% window centred at 224 keV, head 1
OpenR,9, '/home/raw_images/H1_267_2.img'            2% window centred at 267 keV, head 1
OpenR,10,'/home/raw_images/H2_245_15.img'           15% window centred at 245 keV, head 2
OpenR,11,'/home/raw_images/H2_224_2.img'            2% window centred at 224 keV, head 2
OpenR,12,'/home/raw_images/H2_267_2.img'            2% window centred at 267 keV, head 2
OpenR,13,'/home/raw_images/H1_171_245_15.img'       15% windows centred at 171 & 245 keV, head 1
OpenR,14,'/home/raw_images/H2_171_245_15.img'       15% windows centred at 171 & 245 keV, head 2
OpenR,15,'/home/raw_images/H1_209_10.img'           10% window centred at 209 keV, head 1
OpenR,16,'/home/raw_images/H2_209_10.img'           10% window centred at 209 keV, head 2
OpenR,17,'/home/raw_images/H1_211_50.img'           50% window centred at 211 keV, head1
OpenR,18,'/home/raw_images/H2_211_50.img'           50% window centred at 211 keV, head2

H1_171_main   =  ASSOC(1,intARR(128,128))           The images are associated with 128×128
H1_171_lower  =  ASSOC(2,intARR(128,128))           pixel matrices
H1_171_upper  =  ASSOC(3,intARR(128,128))
H2_171_main   =  ASSOC(4,intARR(128,128))
H2_171_lower  =  ASSOC(5,intARR(128,128))
H2_171_upper  =  ASSOC(6,intARR(128,128))
H1_245_main   =  ASSOC(7,intARR(128,128))
H1_245_lower  =  ASSOC(8,intARR(128,128))
H1_245_upper  =  ASSOC(9,intARR(128,128))
H2_245_main   =  ASSOC(10,intARR(128,128))
H2_245_lower  =  ASSOC(11,intARR(128,128))
H2_245_upper  =  ASSOC(12,intARR(128,128))
H1_171_245    =  ASSOC(13,intARR(128,128))
H2_171_245    =  ASSOC(14,intARR(128,128))
H1_209        =  ASSOC(15,intARR(128,128))
H2_209        =  ASSOC(16,intARR(128,128))
H1_211_main   =  ASSOC(17,intARR(128,128))
H2_211_main   =  ASSOC(18,intARR(128,128))

H1_171_main   =     H1_171_main(0)                  The images from detector head 2 are reversed
H1_171_lower  =     H1_171_lower(0)                 in order to turn them the same way around as
H1_171_upper  =     H1_171_upper(0)                 the images from detector head 1
H2_171_main   =  Reverse(H2_171_main(0))
H2_171_lower  =  Reverse(H2_171_lower(0))
H2_171_upper  =  Reverse(H2_171_upper(0))
H1_245_main   =     H1_245_main(0)
H1_245_lower  =     H1_245_lower(0)
H1_245_upper  =     H1_245_upper(0)
H2_245_main   =  Reverse(H2_245_main(0))
H2_245_lower  =  Reverse(H2_245_lower(0))
H2_245_upper  =  Reverse(H2_245_upper(0))
H1_171_245    =     H1_171_245(0)
H2_171_245    =  Reverse(H2_171_245(0))
H1_209        =     H1_209(0)
H2_209        =  Reverse(H2_209(0))
H1_211_main   =     H1_211_main(0)
H2_211_main   =  Reverse(H2_211_main(0))

width171_main =   27.0                              The widths of the windows in keV
width171_lower=    5.0
width171_upper=    5.0
width245_main =   37.0
width245_lower=    5.0
width245_upper=    7.0
width209      =   21.0
width211_main =  107.0
```

The fractions of the high and low energy scatter windows for TEW scatter correction are calculated as described in equations 2-1 and 2-2

```
fraction_H1_171_lower= (Total(H1_171_lower)/width171_lower)/
          ((Total(H1_171_lower)/width171_lower)+(Total(H1_171_upper)/width171_upper))
fraction_H1_171_upper=   1-fraction_H1_171_lower
fraction_H2_171_lower= (Total(H2_171_lower)/width171_lower)/
          ((Total(H2_171_lower)/width171_lower)+(Total(H2_171_upper)/width171_upper))
fraction_H2_171_upper=   1-fraction_H2_171_lower
fraction_H1_245_lower= (Total(H1_245_lower)/width245_lower)/
          ((Total(H1_245_lower)/width245_lower)+(Total(H1_245_upper)/width245_upper))
fraction_H1_245_upper=   1-fraction_H1_245_lower
fraction_H2_245_lower= (Total(H2_245_lower)/width245_lower)/
          ((Total(H2_245_lower)/width245_lower)+(Total(H2_245_upper)/width245_upper))
fraction_H2_245_upper=   1-fraction_H2_245_lower
fraction_H1_211_lower= (Total(H1_171_lower)/width171_lower)/
          ((Total(H1_171_lower)/width171_lower)+(Total(H1_245_upper)/width245_upper))
fraction_H1_211_upper=   1-fraction_H1_211_lower
fraction_H2_211_lower= (Total(H2_171_lower)/width171_lower)/
          ((Total(H2_171_lower)/width171_lower)+(Total(H2_245_upper)/width245_upper))
fraction_H2_211_upper=   1-fraction_H2_211_lower
```

The factors that the scatter images will be multiplied by are calculated

```
weight_H1_171_lower  =   fraction_H1_171_lower*width171_main/width171_lower
weight_H1_171_upper  =   fraction_H1_171_upper*width171_main/width171_upper
weight_H2_171_lower  =   fraction_H2_171_lower*width171_main/width171_lower
weight_H2_171_upper  =   fraction_H2_171_upper*width171_main/width171_upper
weight_H1_245_lower  =   fraction_H1_245_lower*width245_main/width245_lower
weight_H1_245_upper  =   fraction_H1_245_upper*width245_main/width245_upper
weight_H2_245_lower  =   fraction_H2_245_lower*width245_main/width245_lower
weight_H2_245_upper  =   fraction_H2_245_upper*width245_main/width245_upper
weight_H1_211_lower  =   fraction_H1_211_lower*width211_main/width211_lower
weight_H1_211_upper  =   fraction_H1_211_upper*width211_main/width211_upper
weight_H2_211_lower  =   fraction_H2_211_lower*width211_main/width211_lower
weight_H2_211_upper  =   fraction_H2_211_upper*width211_main/width211_upper
weight_209_245       =   width245_main/width209
weight_209_171       =   width171_main/width209
```

The scatter windows are multiplied by the factors calculated above

```
H1_171_lower     =   H1_171_lower   *   weight_H1_171_lower
H2_171_lower     =   H2_171_lower   *   weight_H2_171_lower
H1_171_upper     =   H1_171_upper   *   weight_H1_171_upper
H2_171_upper     =   H2_171_upper   *   weight_H2_171_upper
H1_245_lower     =   H1_245_lower   *   weight_H1_245_lower
H2_245_lower     =   H2_245_lower   *   weight_H2_245_lower
H1_245_upper     =   H1_245_upper   *   weight_H1_245_upper
H2_245_upper     =   H2_245_upper   *   weight_H2_245_upper
H1_211_lower     =   H1_211_lower   *   weight_H1_211_lower
H2_211_lower     =   H2_211_lower   *   weight_H2_211_lower
H1_211_upper     =   H1_211_upper   *   weight_H1_211_upper
H2_211_upper     =   H2_211_upper   *   weight_H2_211_upper
H1_209_245_OSW_A  =  H1_209         *   weight_209_245
H2_209_245_OSW_A  =  H2_209         *   weight_209_245
H1_209_245_OSW_B  =  H1_209         *   weight_209_245/2.0
H2_209_245_OSW_B  =  H2_209         *   weight_209_245/2.0
H1_209_171_OSW   =   H1_209         *   weight_209_171
H2_209_171_OSW    =  H2_209         *   weight_209_171
H1_209_171_EXT    =  H1_209         *   weight_209_171*2.56
H2_209_171_EXT    =  H2_209         *   weight_209_171*2.56
```

The scatter images are deleted from the main images

```
H1_171_TEW_main   =   H1_171_main - H1_171_lower - H1_171_upper
H2_171_TEW_main   =   H2_171_main - H2_171_lower - H2_171_upper
H1_245_TEW_main   =   H1_245_main - H1_245_lower - H1_245_upper
H2_245_TEW_main   =   H2_245_main - H2_245_lower - H2_245_upper
H1_211_TEW_main   =   H1_211_main - H1_211_lower - H1_211_upper
H2_211_TEW_main   =   H2_211_main - H2_211_lower - H2_211_upper
H1_OSW_A_171      =   H1_171_main - H1_209_171_OSW
H2_OSW_A_171      =   H2_171_main - H2_209_171_OSW
H1_OSW_A_245      =   H1_245_main - H1_209_245_OSW_A
H2_OSW_A_245      =   H2_245_main - H2_209_245_OSW_A
H1_OSW_B_171      =   H1_171_main - H1_209_171_OSW
H2_OSW_B_171      =   H2_171_main - H2_209_171_OSW
H1_OSW_B_245      =   H1_245_main - H1_209_245_OSW_B
H2_OSW_B_245      =   H2_245_main - H2_209_245_OSW_B
H1_OSW_EXT_171    =   H1_171_main - H1_209_171_EXT
H2_OSW_EXT_171    =   H2_171_main - H2_209_171_EXT
H1_OSW_EXT_245    =   H1_245_main - H1_209_245_EXT
H2_OSW_EXT_245    =   H2_245_main - H2_209_245_EXT
```

Negative pixel values are prevented

```
For i=0,127 do begin
 For j=0,127 do begin
  If H1_171_TEW_main(i,j) le 0 then H1_171_TEW_main(i,j)=0
  If H2_171_TEW_main(i,j) le 0 then H2_171_TEW_main(i,j)=0
  If H1_245_TEW_main(i,j) le 0 then H1_245_TEW_main(i,j)=0
  If H2_245_TEW_main(i,j) le 0 then H2_245_TEW_main(i,j)=0
  If H1_211_TEW_main(i,j) le 0 then H1_211_TEW_main(i,j)=0
  If H2_211_TEW_main(i,j) le 0 then H2_211_TEW_main(i,j)=0
  If H1_OSW_A_171(i,j)   le 0 then H1_OSW_A_171(i,j)=0
  If H2_OSW_A_171(i,j)   le 0 then H2_OSW_A_171(i,j)=0
  If H1_OSW_A_245(i,j)   le 0 then H1_OSW_A_245(i,j)=0
  If H2_OSW_A_245(i,j)   le 0 then H2_OSW_A_245(i,j)=0
  If H1_OSW_B_171(i,j)   le 0 then H1_OSW_B_171(i,j)=0
  If H2_OSW_B_171(i,j)   le 0 then H2_OSW_B_171(i,j)=0
  If H1_OSW_B_245(i,j)   le 0 then H1_OSW_B_245(i,j)=0
  If H2_OSW_B_245(i,j)   le 0 then H2_OSW_B_245(i,j)=0
  If H1_OSW_EXT_171(i,j)   le 0 then H1_OSW_EXT_171(i,j)=0
  If H2_OSW_EXT_171(i,j)   le 0 then H2_OSW_EXT_171(i,j)=0
  If H1_OSW_EXT_245(i,j)   le 0 then H1_OSW_EXT_245(i,j)=0
  If H2_OSW_EXT_245(i,j)   le 0 then H2_OSW_EXT_245(i,j)=0
 EndFor
EndFor
```

The images from the two photopeaks are fused for window settings OSW_A, OSW_B and OSW_EXT

```
H1_OSW_A        =    H1_OSW_A_171   +   H1_OSW_A_245
H2_OSW_A        =    H2_OSW_A_171   +   H2_OSW_A_245
H1_OSW_B        =    H1_OSW_B_171   +   H1_OSW_B_245
H2_OSW_B        =    H2_OSW_B_171   +   H2_OSW_B_245
H1_OSW_EXT      =    H1_OSW_EXT_171   +   H1_OSW_EXT_245
H2_OSW_EXT      =    H2_OSW_EXT_171   +   H2_OSW_EXT_245
```

The linear attenuation coefficients, acquisition time and phantom thickness used in the geometrical mean attenuation correction

```
my171  =  0.145
my209  =  0.135
my245  =  0.129
acqtime=  1344.0
thickness  =  20.0
```

The images from the two detector heads are fused through geometrical mean attenuation correction

```
GM_NSC_171 =   Sqrt((H1_171_main/acqtime)*(H2_171_main/acqtime))/
               exp(-my171*thickness/2.0)
GM_TEW_171 =   Sqrt((H1_171_TEW_main/acqtime)*(H2_171_TEW_main/acqtime))/
               exp(-my171*thickness/2.0)
GM_NSC_245 =   Sqrt((H1_245_main/acqtime)*(H2_245_main/acqtime))/
               exp(-my245*thickness/2.0)
GM_TEW_245 =   Sqrt((H1_245_TEW_main/acqtime)*(H2_245_TEW_main/acqtime))/
               exp(-my245*thickness/2.0)
GM_NSC_171_245=   Sqrt((H1_171_245/acqtime)*(H2_171_245/acqtime))/
                  exp(-my209*thickness/2.0)
GM_OSW_A_171_245  =  Sqrt((H1_OSW_A/acqtime)*(H2_OSW_A/acqtime))/
                     exp(-my209*thickness/2.0)
GM_OSW_B_171_245  =  Sqrt((H1_OSW_B/acqtime)*(H2_OSW_B/acqtime))/
                     exp(-my209*thickness/2.0)
GM_OSW_EXT_171_245 = Sqrt((H1_OSW_EXT/acqtime)*(H2_OSW_EXT/acqtime))/
                     exp(-my209*thickness/2.0)
GM_NSC_211 =   Sqrt((H1_211_main/acqtime)*(H2_211_main/acqtime))/
               exp(-my209*thickness/2.0)
GM_TEW_211 =   Sqrt((H1_211_TEW_main/acqtime)*(H2_211_TEW_main/acqtime))/
               exp(-my209*thickness/2.0)

End
```

Appendix 2

Program for determination of the spatial resolution

```
PRO Spatial_resolution_Y
```

The processed images are opened

```
OpenR, 1, '/home/processed_images/H1_Y_NSC_171.img'
OpenR, 2, '/home/processed_images/H1_Y_TEW_171.img'
OpenR, 3, '/home/processed_images/H1_Y_NSC_245.img'
OpenR, 4, '/home/processed_images/H1_Y_TEW_245.img'
OpenR, 5, '/home/processed_images/H1_Y_NSC_171_245.img'
OpenR, 6, '/home/processed_images/H1_Y_OSW_B_171_245.img'
OpenR, 7, '/home/processed_images/H1_Y_OSW_EXT_171_245.img'
OpenR, 8, '/home/processed_images/H1_Y_OSW_A_171_245.img'
OpenR, 9, '/home/processed_images/H1_Y_NSC_211.img'
OpenR, 10,'/home/processed_images/H1_Y_TEW_211.img'
```

The images are associated with 256×256 pixel matrices

```
H1_NSC_171        =   ASSOC(1,fltARR(256,256))
H1_TEW_171        =   ASSOC(2,fltARR(256,256))
H1_NSC_245        =   ASSOC(3,fltARR(256,256))
H1_TEW_245        =   ASSOC(4,fltARR(256,256))
H1_NSC_171_245     = ASSOC(5,fltARR(256,256))
H1_OSW_B_171_245   = ASSOC(6,fltARR(256,256))
H1_OSW_EXT_171_245 = ASSOC(7,fltARR(256,256))
H1_OSW_A_171_245   = ASSOC(8,fltARR(256,256))
H1_NSC_211        =   ASSOC(9,fltARR(256,256))
H1_TEW_211        =   ASSOC(10,fltARR(256,256))

H1_NSC_171        =   H1_NSC_171(0)
H1_TEW_171        =   H1_TEW_171(0)
H1_NSC_245        =   H1_NSC_245(0)
H1_TEW_245        =   H1_TEW_245(0)
H1_NSC_171_245   =   H1_NSC_171_245(0)
H1_OSW_B_171_245    =H1_OSW_B_171_245(0)
H1_OSW_EXT_171_245  =H1_OSW_EXT_171_245(0)
H1_OSW_A_171_245    =H1_OSW_A_171_245(0)
H1_NSC_211        =   H1_NSC_211(0)
H1_TEW_211        =   H1_TEW_211(0)
```

One dimensional arrays are created

```
NSC_171_H1        =   fltarr(256)
TEW_171_H1        =   fltarr(256)
NSC_245_H1         =   fltarr(256)
TEW_245_H1        =   fltarr(256)
NSC_171_245_H1     =  fltarr(256)
OSW_B_171_245_H1   =  fltarr(256)
OSW_EXT_171_245_H1 =  fltarr(256)
OSW_A_171_245_H1   =  fltarr(256)
NSC_211_H1        =   fltarr(256)
TEW_211_H1        =   fltarr(256)
```

The ten central columns are put into the one dimensional arrays

```
For j=0,255 do begin
 For k=130,139 do begin
    NSC_171_H1        =   NSC_171_H1 + H1_NSC_171(*,k)
    TEW_171_H1        =   TEW_171_H1 + H1_TEW_171(*,k)
    NSC_245_H1        =   NSC_245_H1 + H1_NSC_245(*,k)
    TEW_245_H1        =   TEW_245_H1 + H1_TEW_245(*,k)
    NSC_171_245_H1    =   NSC_171_245_H1 + H1_NSC_171_245(*,k)
    OSW_B_171_245_H1  =   OSW_B_171_245_H1 + H1_OSW_B_171_245(*,k)
    OSW_EXT_171_245_H1    =   OSW_EXT_171_245_H1 + H1_OSW_EXT_171_245(*,k)
    OSW_A_171_245_H1  =   OSW_A_171_245_H1 + H1_OSW_A_171_245(*,k)
    NSC_211_H1        =   NSC_211_H1 + H1_NSC_211(*,k)
    TEW_211_H1        =   TEW_211_H1 + H1_TEW_211(*,k)
 EndFor
EndFor
```

The values in the arrays are normalised to the maximum value

```
NSC_171_H1       =   NSC_171_H1/MAX(NSC_171_H1)
TEW_171_H1       =   TEW_171_H1/MAX(TEW_171_H1)
NSC_245_H1       =   NSC_245_H1/MAX(NSC_245_H1)
TEW_245_H1       =   TEW_245_H1/MAX(TEW_245_H1)
NSC_171_245_H1    =   NSC_171_245_H1/MAX(NSC_171_245_H1)
OSW_B_171_245_H1  =   OSW_B_171_245_H1/MAX(OSW_B_171_245_H1)
OSW_EXT_171_245_H1 =  OSW_EXT_171_245_H1/MAX(OSW_EXT_171_245_H1)
OSW_A_171_245_H1  =   OSW_A_171_245_H1/MAX(OSW_A_171_245_H1)
NSC_211_H1       =   NSC_211_H1/MAX(NSC_211_H1)
TEW_211_H1       =   TEW_211_H1/MAX(TEW_211_H1)
```

The arrays are renamed

```
l1  =   NSC_171_H1
m1  =   TEW_171_H1
n1  =   NSC_245_H1
o1  =   TEW_245_H1
p1  =   NSC_171_245_H1
q1  =   OSW_B_171_245_H1
r1  =   OSW_EXT_171_245_H1
s1  =   OSW_A_171_245_H1
t1  =   NSC_211_H1
u1  =   TEW_211_H1
```

The column numbers are put into an array

```
Y=intarr(256)
For i=0,255 do begin
   Y(i)= i
Endfor
```

Gaussian functions are fitted to the arrays

```
n_terms=  3
gauss_fitl1   =   GAUSSFIT( Y, l1(*), gauss_coeffl1, NTERMS=n_terms)
gauss_fitm1   =   GAUSSFIT( Y, m1(*), gauss_coeffm1, NTERMS=n_terms)
gauss_fitn1   =   GAUSSFIT( Y, n1(*), gauss_coeffn1, NTERMS=n_terms)
gauss_fito1   =   GAUSSFIT( Y, o1(*), gauss_coeffo1, NTERMS=n_terms)
gauss_fitp1   =   GAUSSFIT( Y, p1(*), gauss_coeffp1, NTERMS=n_terms)
gauss_fitq1   =   GAUSSFIT( Y, q1(*), gauss_coeffq1, NTERMS=n_terms)
gauss_fitr1   =   GAUSSFIT( Y, r1(*), gauss_coeffr1, NTERMS=n_terms)
gauss_fits1   =   GAUSSFIT( Y, s1(*), gauss_coeffs1, NTERMS=n_terms)
gauss_fitt1   =   GAUSSFIT( Y, t1(*), gauss_coefft1, NTERMS=n_terms)
gauss_fitu1   =   GAUSSFIT( Y, u1(*), gauss_coeffu1, NTERMS=n_terms)

DATA   =   '/home/text_files/FWHM_values_Y.txt'
Close,30
OpenW,30,DATA
```

The FWHM values are calculated and put into a text file

```
PrintF,30, "FWHM_values_Y_H1"
printF,30, "FWHM NSC_171 H1:       ", gauss_coeffl1(2)*2.3548*0.234, ' cm'
printF,30, "FWHM TEW_171 H1:       ", gauss_coeffm1(2)*2.3548*0.234, ' cm'
printF,30, "FWHM NSC_245 H1:       ", gauss_coeffn1(2)*2.3548*0.234, ' cm'
printF,30, "FWHM TEW_245 H1:       ", gauss_coeffo1(2)*2.3548*0.234, ' cm'
printF,30, "FWHM NSC_171_245 H1:   ", gauss_coeffp1(2)*2.3548*0.234, ' cm'
printF,30, "FWHM OSW_B_171_245 H1:  ", gauss_coeffq1(2)*2.3548*0.234, ' cm'
printF,30, "FWHM OSW_EXT_171_245 H1:", gauss_coeffr1(2)*2.3548*0.234, ' cm'
printF,30, "FWHM OSW_A_171_245 H1:  ", gauss_coeffs1(2)*2.3548*0.234, ' cm'
printF,30, "FWHM NSC_211 H1:       ", gauss_coefft1(2)*2.3548*0.234, ' cm'
printF,30, "FWHM TEW_211 H1:       ", gauss_coeffu1(2)*2.3548*0.234, ' cm'


END
```

Appendix 3

Appendix of results

Table A1. Calculated values of the system planar sensitivity.

Window setting	*Sensitivity (cps/MBq) Experimental*		*Simulation*	
NSC_171:	83	± 10	82.3	± 0.3
TEW_171:	66	± 8	70.3	± 0.3
NSC_245:	55	± 7	47.3	± 0.2
TEW_245:	44	± 6	39.4	± 0.2
NSC_171_245:	138	± 17	129.6	± 0.4
OSW_A_171_245:	121	± 15	116.5	± 0.3
OSW_B_171_245:	125	± 15	120.3	± 0.3
OSW_EXT_171_245:	116	± 14	111.6	± 0.3
NSC_211:	154	± 19	139.8	± 0.4
TEW_211:	86	± 11	86.0	± 0.3

Table A2. Calculated values of the system spatial resolution.

Window setting	*FWHM (cm) Experimental*	*Simulation*
NSC_171:	1.1	1.0
TEW_171:	1.1	1.0
NSC_245:	1.2	1.0
TEW_245:	1.2	1.0
NSC_171_245:	1.2	1.0
OSW_A_171_245:	1.1	1.0
OSW_B_171_245:	1.1	1.0
OSW_EXT_171_245:	1.1	1.0
NSC_211:	1.2	1.0
TEW_211:	1.1	1.0

Table A3. Calculated contrast values of the 'tumour' relatively to the 'lung'.

Window setting	*Contrast of tumour relative lung Experimental*		*Simulation*	
GM_NSC_171:	0.85	± 0.04	0.85	± 0.08
GM_TEW_171:	0.89	± 0.05	0.89	± 0.09
GM_NSC_245:	0.89	± 0.05	0.89	± 0.10
GM_TEW_245:	0.91	± 0.07	0.92	± 0.12
GM_NSC_171_245:	0.87	± 0.03	0.87	± 0.09
GM_OSW_A_171_245:	0.90	± 0.04	0.90	± 0.10
GM_OSW_B_171_245:	0.89	± 0.04	0.89	± 0.09
GM_OSW_EXT_171_245:	0.93	± 0.05	0.93	± 0.11
GM_NSC_211:	0.85	± 0.03	0.86	± 0.08
GM_TEW_211:	0.99	± 0.07	1.00	± 0.15

Table A4. Calculated contrast values of the 'tumour' relatively to the 'liver'.

Window setting	*Contrast of tumour relative lung* *Experimental*	*Simulation*
GM_NSC_171:	0.71	0.69
GM_TEW_171:	0.75	0.74
GM_NSC_245:	0.75	0.75
GM_TEW_245:	0.78	0.79
GM_NSC_171_245:	0.73	0.71
GM_OSW_A_171_245:	0.76	0.75
GM_OSW_B_171_245:	0.75	0.74
GM_OSW_EXT_171_245:	0.80	0.79
GM_NSC_211:	0.71	0.70
GM_TEW_211:	0.86	0.92

Table A5. Calculated contrast values of the 'tumour' relatively to the 'spine'.

Window setting	*Contrast of tumour relative lung* *Experimental*	*Simulation*
GM_NSC_171:	0.85	0.85
GM_TEW_171:	0.91	0.90
GM_NSC_245:	0.90	0.89
GM_TEW_245:	0.98	0.95
GM_NSC_171_245:	0.87	0.87
GM_OSW_A_171_245:	0.92	0.92
GM_OSW_B_171_245:	0.90	0.90
GM_OSW_EXT_171_245:	0.97	0.96
GM_NSC_211:	0.85	0.84
GM_TEW_211:	1.00	1.00

Table A6. Absolute signal level from ROI

Window setting	*cps/MBq from ROI* *Experimental*	*Simulation*
GM_NSC_171:	38 ± 5	65 ± 4
GM_TEW_171:	31 ± 4	56 ± 4
GM_NSC_245:	25 ± 3	41 ± 3
GM_TEW_245:	20 ± 3	32 ± 3
GM_NSC_171_245:	60 ± 7	100 ± 5
GM_OSW_A_171_245:	53 ± 6	87 ± 5
GM_OSW_B_171_245:	55 ± 7	91 ± 5
GM_OSW_EXT_171_245:	48 ± 6	78 ± 4
GM_NSC_211:	66 ± 8	108 ± 5
GM_TEW_211:	41 ± 5	69 ± 4

Table A7. Absolute signal level from whole image

	cps/MBq from whole image	
Window setting	*Experimental*	*Simulation*
GM_NSC_171:	122 ± 14	140 ± 8
GM_TEW_171:	65 ± 8	84 ± 6
GM_NSC_245:	67 ± 8	67 ± 6
GM_TEW_245:	36 ± 5	42 ± 5
GM_NSC_171_245:	179 ± 21	194 ± 10
GM_OSW_A_171_245:	116 ± 14	143 ± 8
GM_OSW_B_171_245:	125 ± 15	151 ± 9
GM_OSW_EXT_171_245:	85 ± 10	107 ± 7
GM_NSC_211:	237 ± 27	240 ± 11
GM_TEW_211:	68 ± 8	86 ± 7

Table A8. The amount of spill out for the different images.

	Spill out (%)	
Window setting	*Experimental*	*Simulation*
GM_NSC_171:	69 ± 4	53 ± 5
GM_TEW_171:	52 ± 4	34 ± 3
GM_NSC_245:	62 ± 5	39 ± 5
GM_TEW_245:	45 ± 4	25 ± 4
GM_NSC_171_245:	67 ± 3	49 ± 3
GM_OSW_A_171_245:	54 ± 3	39 ± 3
GM_OSW_B_171_245:	56 ± 3	40 ± 3
GM_OSW_EXT_171_245:	44 ± 3	28 ± 2
GM_NSC_211:	72 ± 3	55 ± 4
GM_TEW_211:	39 ± 2	19 ± 2

Table A9. Quantification of the activity in the insert based on the ROI.

	Activity calculated from ROI (MBq)				
Window setting	*Experimental*			*Simulation*	
GM_NSC_171:	4.4 ± 0.6	(-54%)		7.7 ± 0.5	(-21%)
GM_TEW_171:	4.6 ± 0.6	(-53%)		7.7 ± 0.5	(-21%)
GM_NSC_245:	4.5 ± 0.6	(-53%)		8.3 ± 0.6	(-15%)
GM_TEW_245:	4.4 ± 0.6	(-54%)		7.8 ± 0.7	(-20%)
GM_NSC_171_245:	4.2 ± 0.5	(-57%)		7.5 ± 0.4	(-23%)
GM_OSW_A_171_245:	4.2 ± 0.5	(-56%)		7.3 ± 0.4	(-25%)
GM_OSW_B_171_245:	4.3 ± 0.5	(-56%)		7.3 ± 0.4	(-25%)
GM_OSW_EXT_171_245:	4.2 ± 0.5	(-57%)		7.1 ± 0.4	(-27%)
GM_NSC_211:	4.2 ± 0.5	(-57%)		7.5 ± 0.4	(-23%)
GM_TEW_211:	4.7 ± 0.6	(-52%)		7.0 ± 0.4	(-28%)

The values in parentheses are the percentage deviations from the actual activity within the insert phantom. Negative signs indicate underestimation compared to the true activity.

Table A10. *Quantification of the activity in the insert based on the whole image.*

	Activity calculated from the whole image					
Window setting	*Experimental*			*Simulation*		
GM_NSC_171:	14.4	± 1.8	(+47%)	16.5	± 1.0	(+70%)
GM_TEW_171:	9.5	± 1.2	(-2%)	11.6	± 0.9	(+20%)
GM_NSC_245:	12.0	± 1.6	(+23%)	13.6	± 1.2	(+40%)
GM_TEW_245:	8.1	± 1.1	(-17%)	10.5	± 1.2	(+7%)
GM_NSC_171_245:	12.7	± 1.6	(+30%)	14.5	± 0.7	(+49%)
GM_OSW_A_171_245:	9.3	± 1.2	(-4%)	11.9	± 0.7	(+22%)
GM_OSW_B_171_245:	9.7	± 1.2	(0%)	12.2	± 0.7	(+25%)
GM_OSW_EXT_171_245:	7.4	± 0.9	(-24%)	9.8	± 0.7	(0%)
GM_NSC_211:	15.0	± 0.8	(+54%)	16.6	± 0.8	(+70%)
GM_TEW_211:	7.7	± 1.0	(-21%)	8.7	± 0.7	(-11%)

The values in parentheses are the percentage deviation from the actual activity within the insert phantom.

Appendix 4

Experimental images

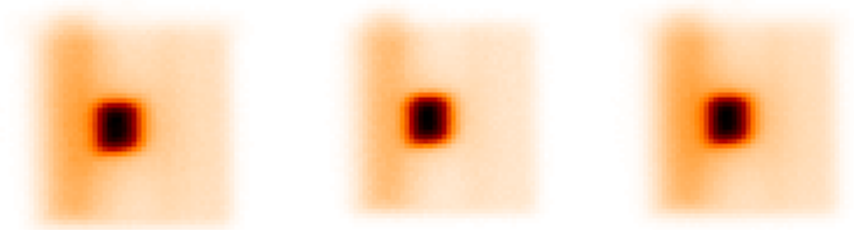

***(a)**. GM_NSC_171* ***(b)**. GM_NSC_245* ***(c)**. GM_NSC_211.*

***Figure A1**. The attenuation corrected experimental images when using one main energy window before scatter correction (GM denotes Geometrical Mean attenuation correction).*

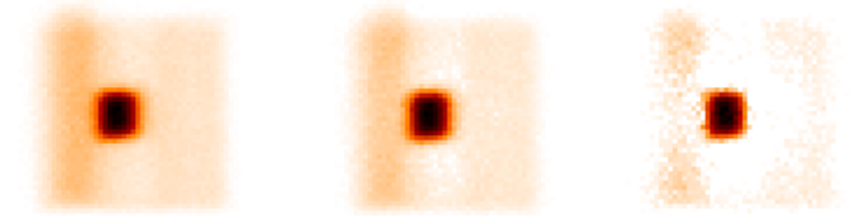

***(a)**. GM_TEW_171* ***(b)**. GM_TEW_245* ***(c)**. GM_TEW_211*

***Figure A2**. The experimental attenuation- and TEW scatter corrected images.*

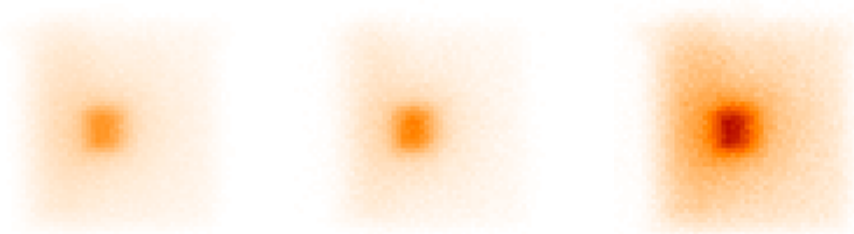

***(a).** TEW_171* ***(b).** TEW_245* ***(c).** TEW_211*

***Figure A3**. The scatter images deleted from the experimental images when using one main energy window and TEW scatter correction.*

***(d)**. GM_NSC_171_245, attenuation corrected image before scatter correction*

***(e)**.**GM**_OSW_A_171_245, attenuation- and scatter corrected image*

***(h)**. GM_OSW_B_171_245, attenuation- and scatter corrected image*

***(k)**. GM_OSW_EXT_171_245, scatter corrected*

***(f)**. GM_OSW_A_171_245, scatter image deleted from the 171 keV image*

***(i)**. GM_OSW_B_171_245, scatter image deleted from the 171 keV image*

***(l)**. GM_OSW_EXT_171_245, scatter image deleted from the 171 keV image*

***(g)**. GM_OSW_A_171_245, scatter image deleted from the 245 keV image*

***(j)**. GM_OSW_B_171_245, scatter image deleted from the 245 keV image*

***(m)**. GM_OSW_EXT_171_245, scatter image deleted from the 245 keV image*

***FigureA4.** The experimental images obtained with the OSW window settings with corresponding correction methods and the scatter images deleted.*